

Coordinated chemical and microstructural analyses of presolar silicate grains from AGB/RGB stars and supernovae in the CO3.0 chondrite Dominion Range 08006

Laura B. Seifert¹, Pierre Haenecour¹ and Thomas J. Zega^{1,2}

¹Lunar and Planetary Laboratory
University of Arizona
1629 E. University Blvd.
Tucson AZ 85721

²Department of Materials Science and Engineering
University of Arizona
1235 E. James E. Rogers Way
Tucson AZ 85721

Correspondence to: lseifert@lpl.arizona.edu
Phone: 517-294-3490

A manuscript in preparation for submission to Meteoritics & Planetary Science

Keywords: meteorites, presolar grains, silicates, FIB-SEM, transmission electron microscopy, secondary ion mass spectrometry, AGB/RGB stars, supernovae

Abstract

We report the structural and chemical analyses of six presolar silicate grains identified in situ in the CO3.0 carbonaceous chondrite Dominion Range (DOM) 08006. Two of the grains have O-isotopic compositions consistent with origins in the circumstellar envelopes of low-mass ($<2M_{\odot}$) Asymptotic Giant Branch (AGB)/Red Giant branch (RGB) stars, although without Mg-isotopic data, origins in supernovae (SNe) cannot be ruled out. The other four grains have O-isotopic compositions consistent with origins in the ejecta of type-II SNe. Transmission electron microscopy (TEM) analyses reveal that all grains are crystalline (single crystal or polycrystalline) and have varied compositions. The analyzed AGB/RGB grains include an Fe-rich crystalline olivine with an Fe-sulfide inclusion and a chemically zoned olivine grain that also contains an Fe-oxide rim. The grains derived from SNe include two polycrystalline assemblages with structures that overlap with both olivine and pyroxene, an assemblage composed of both a single crystal of forsterite as well as polycrystalline forsterite, and an orthopyroxene grain with an embedded Fe-sulfide crystal. The thermodynamic origins of both AGB/RGB and SN grains are also diverse. The structure and compositions of two grains are consistent with equilibrium thermodynamic predictions of condensation, whereas four are not, suggesting formation through nonequilibrium or multi-step processes. Our observations of presolar silicate grains suggest that the circumstellar envelopes of AGB/RGB stars and the ejecta of SNe can produce grains with comparable structures and compositions.

Introduction

During the latter stages of stellar evolution, dust is produced in circumstellar envelopes and in the ejecta of stellar explosions such as supernovae (SNe). These circumstellar dust grains are transported away from the star, enter the interstellar medium (ISM), and can be incorporated into newly forming stellar and planetary systems. A portion of grains that condensed in stellar environments traveled through the ISM and were incorporated into our solar system. Some of these ‘presolar’ grains survived solar-system formation and are identifiable by their anomalous isotopic compositions in primitive solar-system materials such as meteorites, micrometeorites, interplanetary dust particles, and more recently, cometary samples returned by the NASA Stardust mission. Recorded within the chemistry and crystal structure of these materials are the nucleosynthetic processes and thermodynamic properties of the environments in which they

condensed (e.g., Zinner 2014; Floss & Haenecour 2016; Nittler & Ciesla 2016). Thus, analysis of the isotopic and chemical compositions, as well as the crystal structure of circumstellar grains can therefore provide ground-truth information on nucleosynthetic processes, the thermodynamic conditions in circumstellar environments and stellar explosions, as well as their subsequent transport and alteration histories in the ISM and on meteorite parent bodies.

Silicates are the most abundant type of dust present in circumstellar envelopes of evolved O-rich stars and the ISM (e.g., Kemper et al. 2004; Speck et al. 2000; Tielens et al. 1998). The majority (>90%) of silicate dust formed in circumstellar envelopes is believed to be amorphous with Fe-bearing olivine compositions, though some circumstellar envelopes have more substantial fractions of crystalline dust (Tielens et al. 1998; Speck et al. 2000; Molster & Kemper 2005). Similarly, observations have also suggested that silicates in the ISM are also Fe-bearing and mainly (>99%) amorphous due to ion radiation, shock waves from SNe, and grain-grain collisions (Kemper et al. 2004; Jones & Nuth 2011). Of the fraction that are crystalline, observations suggest forsteritic (Mg_2SiO_4) compositions, but a small portion occur as pyroxenes such as diopside ($\text{CaMgSi}_2\text{O}_6$) and enstatite (MgSiO_3) (Kemper et al. 2004).

Astronomical observations also provide some insight into the composition of dust in the ejecta of SNe and suggest an abundance of amorphous silicates (e.g., Arendt et al. 1999; Rho et al. 2008, 2009). For example, infrared (IR) observations of the Cassiopeia A (Cas A) supernova (SN) remnant show clear evidence for dust formation (Arendt et al. 1999). The dust mass of Cas A is estimated to be 0.020 to 0.054 solar mass (M_\odot) and infrared spectrograph (IRS) spectra of Cas A obtained by Spitzer Space Telescope observations show features consistent with abundant Mg-silicates as well as other species including SiO_2 , SiC, metallic Fe, oxides, and sulfides (Rho et al. 2008; Arendt et al. 2014). Similarly, Spitzer observations of the young SN remnant 1E0102-72.3 show evidence for newly formed dust, with dust mass estimated to be 0.007 to 0.015 M_\odot and spectral features consistent with MgSiO_3 and Si are observed (Rho et al. 2009).

Presolar grains are among the building blocks of our solar system and are therefore of particular interest for models of solar-system formation. A SN shock was suggested to have triggered solar-system formation (Cameron & Truran 1977), and the presence of some short-lived radionuclides in the early solar system suggests contribution of material from a nearby SN (e.g., MacPherson et al. 1995; Tachibana & Huss 2003; Busso et al. 2003; Nittler & Dauphas 2006). The contribution of material from a nearby SN explosion is also supported by isotopic evidence in presolar grains.

Such evidence includes the initial presence of short-lived ^{44}Ti and ^{49}V (Amari et al. 1992, 1995; Hoppe et al. 1996, 2000; Nittler et al. 1996; Hoppe & Besmehn 2002; Besmehn & Hoppe 2003) which have origins in SNe (Timmes et al. 1996), ^{28}Si excesses, and large inferred $^{26}\text{Al}/^{27}\text{Al}$ ratios which cannot be explained by other stellar origins (e.g., Amari et al. 1995; Hoppe et al. 1996, 2000; Nittler et al. 1995; Lin et al. 2002). Additionally, the relative abundances of SN oxide and silicate grains varies among different primitive materials. SN grains make up $\sim 25\text{-}30\%$ of the presolar oxide and silicate population in micrometeorites and interplanetary dust particles, whereas they compose only $\sim 10\%$ of presolar oxides and silicates in primitive carbonaceous chondrites (Floss & Haenecour 2016). Work by Hoppe et al. (2015) notes that there could be a correlation between grain size and the fraction of O-rich SN grains in primitive meteorites, where the ≤ 150 nm size fraction of SN grains in their study made up $\sim 33\%$ of the total number of grains. This heterogeneous distribution of SN oxide and silicate grains among primitive planetary materials is thought to suggest that grains were injected into the early solar nebula from a nearby SN and incorporated in varied amounts into parent bodies forming in different parts and/or at different times in the solar nebula (Yada et al. 2008).

Detailed chemical and mineralogical analyses of presolar silicates from AGB stars, RGB stars, and SNe using transmission electron microscopy (TEM) have provided insight into their origins. Studies reveal structures and morphologies that include amorphous grains, single crystals, aggregates, and polycrystalline assemblages, with compositions including olivine, pyroxene, and intermediate compositions between the two (Messenger et al. 2003, 2005; Floss et al. 2006; Nguyen et al. 2007, 2010, 2016; Vollmer et al. 2007, 2009, 2013; Stroud et al. 2013, 2014; Zega et al. 2020; Haenecour et al. 2020). These studies reveal complex formation histories, with evidence for equilibrium condensation suggested by single, stoichiometric crystals, deviations from equilibrium suggested by nonstoichiometric, amorphous, Fe-rich phases, and potentially multistep condensation suggested by polycrystalline assemblages. Evidence for secondary alteration processes in the ISM, solar nebula, and on the parent body are also observed in some grains (e.g., Vollmer et al. 2009; Nguyen et al. 2010, 2016; Floss and Stadermann 2012; Leitner et al. 2016; Zega et al. 2020).

The majority of silicate grains analyzed for their detailed structure and chemistry are derived from AGB/RGB origins. SN silicates are thought to comprise $\sim 10\%$ of anomalous grains in meteorites (Haenecour et al. 2018), though recent work suggests this abundance could be much

higher (13% to 20%), as some Group-1 and Group-2 grains originally thought to be from AGB/RGB origins could be from SNe (Leitner & Hoppe 2019; Verdier-Paoletti et al. 2019; Hoppe et al. 2021). Therefore, there is a need for further analyses of SN silicates in order to understand the thermodynamic conditions of dust formation within the ejecta of SNe and their subsequent transport and preservation in solar-system materials. Here we report the coordinated analyses of six presolar silicate grains, two of which are thought to have formed in the circumstellar envelopes of AGB stars, and four of which are thought to have formed in the ejecta of SNe. The silicate grains were identified in situ in order to compare the structure and chemistry of grains derived from different stellar origins from the same meteorite and to understand their thermodynamic origins. Initial results were reported in Seifert et al. (2018, 2019, 2020).

Samples and Experimental Methods

A petrographic thin section of the CO3.0 Dominion Range (DOM) 08006 carbonaceous chondrite obtained from the meteorite curatorial facility at NASA Johnson Space Center was examined. DOM 08006 is composed of an unequilibrated mixture of anhydrous silicates, metal, and sulfides (Davidson et al. 2019) and is classified as one of the most pristine meteoritic samples available for study due to its lack of evidence of alteration processes. DOM 08006 contains one of the highest abundances of O-rich presolar grains reported to date in meteorites (~257 ppm, Haenecour et al. 2018; Nittler et al. 2018; Davidson et al. 2019), similar to abundances reported in a recent study of Asuka 12169 (~236 ppm, Nittler et al. 2021). Raster-ion imaging of select matrix regions and fine-grained rims around chondrules (FGRs) was performed with the Cameca NanoSIMS 50 at Washington University in St. Louis and previously reported by Haenecour et al. (2018). That work identified 55 presolar grains containing anomalous oxygen isotopic compositions. Following the NanoSIMS measurements, the grains were also measured with the PHI 700 Auger nanoprobe at Washington University in St. Louis, where quantitative major element compositions of the grains were derived from Auger spectra. Auger maps were acquired for select grains based on their isotopic and elemental compositions. Information on the NanoSIMS and Auger analysis can be found in Haenecour et al. (2018). We selected six of these grains based on their size ($100 \text{ nm} < x < 1 \text{ }\mu\text{m}$) and suggested AGB/RGB or SN origins, as indicated by their isotopic compositions, for detailed analysis using TEM.

Electron transparent cross-sections (<100 nm in projected thickness) of the selected grains were prepared for detailed structural and chemical analysis using the Thermo Fisher Scientific (formerly FEI) Helios G³ focused-ion beam scanning-electron microscope (FIB-SEM) located in the Kuiper Materials Imaging and Characterization Facility (KMICF) at the Lunar and Planetary Laboratory (LPL), University of Arizona. The procedure for producing electron-transparent cross sections of presolar grains was described in many papers (Stroud et al. 2004; Nguyen et al. 2007, 2016; Vollmer et al. 2007, 2009, 2013; Zega et al. 2007, 2011, 2014, 2015, 2020; Holzapfel et al. 2009; Leitner et al. 2012a, 2016; Haenecour et al. 2019, 2020). Briefly, we first go through an alignment procedure to ensure that we capture the anomalous region of interest, initially identified with NanoSIMS, in our FIB transect. The ImageAlign software (e.g., Floss et al. 2006; Floss & Stadermann 2009a, 2012) is used to correlate and align NanoSIMS and Auger data, including both ion and secondary electron (SE) images, with SE images from the FIB-SEM to confirm the location of the anomalous grain. The ImageAlign application works by aligning features between two images. All the NanoSIMS raster ion images and SE Auger images are imported into the software and morphologic features are matched between the two datasets until they are aligned. Once the images are aligned, we trace the O-isotope anomaly in the NanoSIMS image and the corresponding area is automatically traced in the SE image. We repeat this process a second time with two SE images from the Auger nanoprobe, one with the traced O-anomaly and a higher resolution SE image to ensure precise location of the anomaly. The alignment software is capable of aligning images of different magnification and/or orientation. Thirdly, the alignment procedure is repeated with SE images from the Auger nanoprobe and the higher resolution SE image from the FIB-SEM. Finally, these alignments are then confirmed one more time by manually overlaying the SE NanoSIMS images, SE FIB-SEM images, and O-isotope maps (see supporting data Fig. 9-12). We note that this alignment is not only completed by one person, but is a group effort and includes extensive discussion of the best plan for FIB extraction. Next, using the electron beam in the FIB, we deposited a protective Pt fiducial marker on top of the grain as well as 100 nm thick markers on either side of the grain fiducial. The purpose of the fiducial markers are to: (i) provide an initial protective layer for the grains of interest prior to final deposition of the C capping layer; (ii) mark their location in cross section as an endpoint indicator for ion milling; and (iii) facilitate identification of the grain in cross section in the TEM. We note that the NanoSIMS and Auger analyses confirmed that the presolar grain was not completely sputtered during the NanoSIMS

measurements. Prior to FIB extraction and subsequent TEM analyses, the crystallinity, shape, and the extent to which the anomalous region permeates below the surface of the section are unknown. We therefore do not presume the extent of the carrier of the isotopic anomaly below the sample surface or whether it is a single phase, multiple grains, or polycrystalline. The correct placement of the Pt fiducial markers is therefore essential to locating the anomalous region of interest in the TEM. Following the deposition of the Pt fiducial markers, a C capping layer ($\sim 3 \mu\text{m}$ thick) was deposited over the Pt markers using the Ga^+ ion beam to further protect the grain from ion implantation and radiation damage during the ion milling process. Generally, C is deposited transecting the longest dimension of the grains to maximize the cross-sectional area that we can analyze in the TEM. Cross sectioning involved staircase cuts previously described in the aforementioned papers, in situ extraction, and thinning to $< 100 \text{ nm}$.

The FIB sections were analyzed using the Hitachi HF5000 scanning TEM (S/TEM) in the KMICF at LPL. The HF5000 is equipped with a cold-field emission gun, a 3rd-order spherical-aberration corrector for STEM mode, bright-field (BF), dark-field (DF), and SE STEM detectors, and an Oxford Instruments X-Max N 100 TLE EDS system with dual 100 mm^2 windowless silicon-drift detectors providing a large solid angle ($\Omega = 2.0 \text{ sr}$) for rapid EDS mapping of samples in minutes instead of hours. It is also equipped with a Gatan OneView $4\text{k} \times 4\text{k}$ pixel CMOS camera for the acquisition of TEM images and electron-diffraction patterns.

Grain composition was obtained through EDS mapping and standardless quantification based on the Cliff-Lorimer method (Cliff & Lorimer 1975) with theoretical correction (k) factors. Information on the long-range atomic order and crystal structure was determined using selected-area electron-diffraction (SAED) patterns. All SAED patterns were measured manually with Adobe Photoshop and with the Crystallographic Image Processing Software Package (CRISP, Hovmöller 1992) based on calibrated camera constants. Additionally, the indexing of experimental SAED patterns were verified by comparison to simulated diffraction patterns using the CrystalMaker software package.

Results

DOM-49

The O-isotopic compositions of all grains were reported in Haenecour et al. (2018), but we note them here to place constraints on their stellar origins. NanoSIMS analysis shows that DOM-

49 is enriched in ^{17}O relative to solar-system values with $^{17}\text{O}/^{16}\text{O} = 5.3 \pm 0.2 (\times 10^{-4})$ and $^{18}\text{O}/^{16}\text{O} = 2.05 \pm 0.04 (\times 10^{-3})$. It plots in the Group-1 field of O-rich presolar grains (Fig. 1) as defined by Nittler et al. (1997, 2008) and contains an oval shaped O-anomaly measuring 235×195 nm (Fig. 2a, arrow). Auger nanoprobe analysis shows that the composition of the grain is consistent with a ferromagnesian silicate. Additional information on major-element compositions for each grain can also be found in Haenecour et al. (2018).

STEM imaging of the region below the Pt marker reveals an oval-shaped domain, indicated by a dashed line in Fig. 2b with orthogonal dimensions of 170×83 nm. HAADF contrast is mostly uniform except for a relatively brighter rounded feature in the center measuring 30×27 nm, indicated by an arrow in Fig. 2c. EDS mapping of the bulk of the domain reveals spatial correlations among Fe, O, Si, Mg, and also Ca and Al. (Fig. 2d-g and j-k, respectively). Mg is concentrated in the left and right portions of the domain and Ca is concentrated at the top and right. The bright feature located in the middle of the domain reveals spatial correlations among Fe, Ni, and S (Fig. 2d, h-i). Comparison of the HAADF (Fig. 2c) and SE (not shown) images of the Fe, Ni, S region suggest that the feature is not on the surface. We were not able to obtain an SAED pattern from this region due to its small size, however, the elemental composition extracted from an EDS spectrum can be found in Table 1. Zone-axis SAED patterns were obtained from the right and left sides of DOM-49, indicated by the dashed circles in Fig. 2c and indexing is consistent with a single crystal of olivine (Fig. 2l-m). Standardless quantification of an EDS spectrum extracted from the grain indicates an Fe-rich olivine composition of $(\text{Mg}_{0.44}, \text{Fe}_{1.03}, \text{Ca}_{0.05}, \text{Ni}_{0.09}, \text{Al}_{0.1})(\text{Si}_{1.12})\text{O}_4$ (Table 1).

DOM-59

NanoSIMS analysis of DOM-59 reveals a crescent-shaped O-anomaly measuring 310×390 nm (Fig. 3 a-b). It is characterized by enrichment in ^{17}O and depletion in ^{18}O relative to solar-system values, with $^{17}\text{O}/^{16}\text{O} = 11.6 \pm 0.5 (\times 10^{-4})$ and $^{18}\text{O}/^{16}\text{O} = 0.69 \pm 0.03 (\times 10^{-3})$ and plots in the Group-2 field (Fig. 1). Auger nanoprobe mapping shows correlations among Mg, Fe, Si and O suggesting that the grain is a ferromagnesian silicate (Fig. 3d-h).

STEM imaging below the Pt fiducial marker reveals an irregularly shaped grain with orthogonal dimensions of 670×596 nm (Fig. 4a-b). HAADF imaging shows a brighter contrast rim (Fig. 4b) that is visible by a textural change outside the grain, as indicated by arrows in Fig.

4a. In an effort to get the FIB section as thin as possible for TEM analysis, part of the capping layer and grain were milled through during final thinning. However, the majority of the grain remained undamaged and half of the grain remained covered by the capping layer. EDS mapping reveals spatial correlations among several elements. The bulk of the grain contains spatial correlations among Mg, Si, and O (Fig. 4d-f), whereas the center of the grain contains spatial correlations among O, Si and Ca (Fig. 4d-e,g) and lesser amounts of Mg (Fig. 4f). The rim shows spatial correlations between Fe and O with minor Si and Mg (Fig. 4c-f). We note that the overall FIB section of DOM-59 has a more compact structure than the other FIB sections of DOM 08006. We observe heterogeneous distributions of iron in the section with vein-like structures that appear to surround aggregates of grains. SAED patterns acquired across DOM-59 indicate that the grain is crystalline and indexing of a zone-axis pattern is consistent with forsterite (a representative pattern is shown in Fig. 4h). We were not able to obtain a distinct SAED pattern from the Ca-rich center of DOM-59. An EDS spectrum was extracted from the Mg-rich surface region and standardless quantification indicates a forsterite composition with $(\text{Mg}_{1.89}, \text{Fe}_{0.09})(\text{Si}_{1.01})\text{O}_4$ (Table 1). An EDS spectrum was also extracted from the Ca-rich core of the grain and standardless quantification suggests a Ca-rich olivine composition with $(\text{Mg}_{1.62}, \text{Fe}_{0.03}, \text{Ca}_{0.27})(\text{Si}_{1.04})\text{O}_4$ (Table 1).

DOM-22

NanoSIMS analysis reveals an oval-shaped O-anomaly with orthogonal dimensions of 195×195 nm indicated by an arrow in Fig. 5a. The anomaly is characterized by enrichment in ^{18}O relative to solar-system values with $^{17}\text{O}/^{16}\text{O} = 3.8 \pm 0.2 (\times 10^{-4})$ and $^{18}\text{O}/^{16}\text{O} = 2.47 \pm 0.05 (\times 10^{-3})$ and plots in the Group-4 field (Fig. 1). Auger nanoprobe analysis indicates a ferromagnesian silicate composition (Haenecour et al. 2018).

STEM imaging shows that DOM-22 is not a discrete grain, precluding identification of a single-phase carrier of the O-isotope anomaly. We therefore consider the region below the Pt fiducial marker as the O-anomalous presolar ‘grain’ DOM-22 (Fig. 5b-d). HAADF images reveal a bright, high-contrast, elongated feature in the center of the field of view (indicated by arrow and dashed outline in Fig. 5c) suggesting a higher average atomic number material than the bulk, measuring 118×50 nm. EDS mapping below the Pt fiducial marker reveals that the bulk of the domain spatially correlates with Fe, O, Si, Mg, with minor Al (Fig. 5e-h, k). The high-contrast

region in the center of the field of view shows correlations among Fe, Ni, and S (Fig. 5e, i-j). EDS also reveals that other parts of the domain spatially correlate with Fe, Ni, and S, however, their small sizes preclude single-crystal SAED patterns from being acquired. SAED patterns were acquired across DOM-22 and indicate that the bulk of the domain is fine-grained, polycrystalline, and has d-spacings that overlap with both olivine and pyroxene (Table 2, Fig. 5m). Standardless quantification of EDS spectra from the fine-grained ferromagnesian silicate domain indicates a composition of $(\text{Mg}_{3.48}, \text{Fe}_{1.52}, \text{Ni}_{0.13})(\text{Si}_{3.32}, \text{Al}_{0.15})\text{O}_{12}$ (Table 1). Due to the overlapping d-spacings with olivine and pyroxene, the cation composition was quantified based on 12 O atoms, which is the least common multiple of the three and four oxygens per formula unit specific to pyroxene and olivine, respectively. The calculated composition most closely matches a mixture of olivine and pyroxene. In comparison, a zone-axis SAED pattern was acquired from the high-contrast Fe, Ni, S rich feature (Fig. 5n) in the center of the field of view and can be indexed to pentlandite. Standardless quantification of the pentlandite crystal indicates a composition of $(\text{Fe}_{6.68}, \text{Ni}_{3.22})\text{S}_{6.69}$ (Table 1). Comparison of the pentlandite crystal with the SE image shows that a portion appears to protrude from the surface of DOM-22 (indicated by arrow and dashed outline in Fig. 5d). However, the entirety of the feature observed in the BF and HAADF images is not visible on the surface, which suggests the feature permeates through the polycrystalline domain DOM-22. The NanoSIMS measurements of DOM-22 only provide isotopic information for grains located at the surface of the meteorite thin section. The pentlandite crystal occurs below the surface that NanoSIMS measured, therefore precluding the definitive identification of the pentlandite as a presolar grain within the anomalous region of DOM-22.

DOM-35

NanoSIMS analysis reveals an oval shaped O-anomaly measuring 235×235 nm, indicated by an arrow in Fig. 6a. It is characterized by enrichments in both ^{17}O and ^{18}O relative to solar system values with $^{17}\text{O}/^{16}\text{O} = 4.0 \pm 0.2 (\times 10^{-4})$ and $^{18}\text{O}/^{16}\text{O} = 3.34 \pm 0.07 (\times 10^{-3})$. The isotopic composition of DOM-35 plots in the Group-4 field (Fig. 1). Auger nanoprobe analysis indicates a ferromagnesian silicate composition (Haenecour et al. 2018).

STEM imaging does not reveal a grain with distinct boundaries, and so we evaluate the domain located directly below the Pt fiducial marker. The domain measures of 264×210 nm in orthogonal dimensions (Fig. 6b-c). EDS mapping shows spatial correlations among Fe, Si, O, Mg and

localized Ca (Fig. 6d-h). A zone-axis SAED pattern was acquired from the left portion of the domain and is consistent with a single crystal of forsterite (Fig. 6j). In comparison, an SAED pattern acquired from the right portion is polycrystalline with d-spacings consistent with forsterite (Table 2, Fig. 6k). EDS spectra were extracted from both the left and right parts of DOM-35. Standardless quantification indicates a Mg-rich forsterite with a composition of $(\text{Mg}_{1.66}, \text{Fe}_{0.17}, \text{Ca}_{0.03}, \text{Al}_{0.05})(\text{Si}_{1.03})\text{O}_4$ for the single crystal region on the left side and a more Fe-rich forsterite with a composition of $(\text{Mg}_{1.65}, \text{Fe}_{0.27}, \text{Al}_{0.06})(\text{Si}_{1.00})\text{O}_4$ for the polycrystalline region on the right side (Table 1).

DOM-39

NanoSIMS analysis of DOM-39 reveals a circular O-anomaly measuring 275 nm in diameter, indicated by arrows in Fig. 7a-b. It is characterized by enrichments in both ^{17}O and ^{18}O , with $^{17}\text{O}/^{16}\text{O} = 6.4 \pm 0.3 (\times 10^{-4})$ and $^{18}\text{O}/^{16}\text{O} = 2.64 \pm 0.07 (\times 10^{-3})$. The O-isotopic composition of DOM-39 plots near to the boundary between Groups 1 and 4, but is closer to the Group-4 field (Fig. 1), which is consistent with the classification described in Haenecour et al. (2018). Auger nanoprobe analysis reveals a ferromagnesian silicate composition (Haenecour et al. 2018).

STEM imaging of the region below the Pt fiducial marker reveals an oval-shaped domain, indicated by dashed line in Fig. 7c, with orthogonal dimensions of 296×160 nm (Fig. 7c-e). BF and HAADF images show a high-contrast footprint-shaped feature in the upper-left corner of the field of view that extends into the top left part of the domain and measures $\sim 50 \times 130$ nm (Fig. 7c-d). We note that the footprint feature is too small to be distinguishable on NanoSIMS maps at the resolution used for routine imaging (~ 100 nm spatial resolution) of the meteorite thin section, thus precluding isotopic measurements and definitive determination of its presolar origins. However, comparison with the SE image (Fig. 7e) indicates that the footprint-shaped feature is not on the surface of the cross-section exposed by FIB and appears to be within the anomalous region. Additionally, this FIB section was thinned twice due to Pt redeposition over the region of interest. After both thinning sessions, the feature does not appear on the surface and therefore is included within the thickness of the section. We note that the random orientation of the footprint feature observed in the TEM images is dependent on multiple factors including how the thin sections were cut from the original meteorite sample and also how we chose to section the anomalous region.

The footprint-shaped feature also contains a rim (cf., Fig. 7c-d, e). EDS mapping of DOM-39 reveals spatial correlations among Fe, O, Si, Mg, with minor Al, (Fig. 7f-i,l). The footprint shaped region correlates strongly with Fe, and contains local Ni and S concentrated at its center (Fig. 7f, j-k). The rim around the footprint spatially correlates with Fe and O (Fig. 7f-g, supporting data fig. 13c-d). A zone-axis SAED pattern was acquired from the center of DOM-39 and indexes to orthopyroxene (Fig. 7m). An EDS spectrum was extracted from the grain and standardless quantification is consistent with a composition of $(\text{Mg}_{0.38}, \text{Fe}_{0.52}, \text{Ni}_{0.1})(\text{Al}_{0.09}, \text{Si}_{0.93})\text{O}_3$ (Table 1). Zone-axis SAED patterns were also obtained across the footprint region (see supporting data Fig. 13i-k) and measurement of such patterns reveal d-spacings close to the pyrrhotite-6C structure (Fig. 7n, Table 2). However, standardless quantification of the footprint region is not consistent with pyrrhotite stoichiometry, as it is enriched in Fe and depleted in S with a composition $(\text{Fe}_{1.37}, \text{Ni}_{0.22})\text{S}_{0.405}$ (Table 1). Henceforth, we refer to the crystal as an Fe-sulfide.

DOM-50

NanoSIMS analysis of DOM-50 reveals a circular O-anomaly measuring 195 nm, indicated by arrow in Fig. 8a. DOM-50 is characterized by enrichment in ^{18}O , with $^{18}\text{O}/^{16}\text{O} = 2.56 \pm 0.05 (\times 10^{-3})$ and $^{17}\text{O}/^{16}\text{O} = 3.6 \pm 0.2 (\times 10^{-4})$ and the isotopic composition plots in the Group-4 field (Fig. 1). Auger nanoprobe analysis reveals a ferromagnesian silicate composition (Haenecour et al. 2018). STEM imaging of the region below the Pt fiducial marker reveals an oval-shaped domain, indicated with dashed line in Fig. 8b, with orthogonal dimensions of 187×91 nm (Fig. 8b-c). EDS mapping of the bulk of the domain reveals spatial correlations among Fe, O, Si (Fig. 8d-f), and localized Mg, as well as a significant amount of Pt redeposition covering the top half of DOM-50 (Fig. 8g-h). The maps indicate that Fe and O are concentrated towards the bottom of the domain and Si and Mg are concentrated towards the right side. A SAED pattern was acquired from the center of the domain, indicating DOM-50 is polycrystalline with d-spacings that overlap with both olivine and pyroxene (Table 2, Fig. 8i). Standardless quantification of the polycrystalline region extracted from an EDS spectrum based on 12 O atoms is consistent with a composition of $(\text{Mg}_{2.05}, \text{Fe}^{2+}_{4.22}, \text{Ca}_{0.10}, \text{Ti}_{0.18})(\text{Si}_{1.78}, \text{Fe}^{3+}_{1.72})\text{O}_{12}$ (Table 1).

Discussion

The isotopic compositions of oxygen-rich presolar grains define broad trends in three-oxygen isotope space that can be reproduced by nucleosynthetic models of stellar evolution (Nittler et al. 1997). The comparison of the isotopic data to such models has therefore led to detailed insights into nucleosynthesis in RGB, AGB stars, as well as stellar explosions such as novae and SNe (e.g., Boothroyd et al. 1994; Nittler et al. 1997, 2008; Boothroyd & Sackmann 1999; Nollett et al. 2003; Meyer & Zinner 2006; Lugaro et al. 2017; Leitner & Hoppe 2019). Comparison of grain isotopic data with nucleosynthetic models of stellar evolution is used to determine the type, mass, and metallicity of the progenitor star from which the grains originated in addition to mixing processes that occurred within them (Boothroyd et al. 1994; Boothroyd & Sackmann 1999). Similarly, the isotopic compositions of grains derived from stellar explosions are reproducible with nucleosynthetic models of SNe (Choi et al. 1998; Nittler et al. 2008; Nguyen & Messenger 2014a).

O-rich circumstellar grains can be divided into four groups based on their O-isotopic compositions, which are indicative of different stellar origins. Group-1 grains are characterized by enrichment in ^{17}O relative to solar-system values and many also have slight depletions in ^{18}O . These Group-1 grains are thought to have condensed in the circumstellar envelopes of low-mass RGB or AGB stars experiencing dredge-up processes (Nittler et al. 1997; Boothroyd & Sackmann 1999; Nollett et al. 2003). Dredge up involves convective mixing that transports the products of main-sequence nucleosynthesis to the circumstellar envelope. The nuclides make their way to the surface of the star where solid dust grains can condense according to their thermodynamic stabilities, incorporating the products from main-sequence nucleosynthesis. The O-isotopic compositions of grains derived from AGB/RGB origins can be used to trace the mass and metallicity of their progenitor stars by comparison with model predictions (Boothroyd et al. 1994; Boothroyd & Sackmann 1999). The $^{17}\text{O}/^{16}\text{O}$ ratio is related to stellar mass, and the $^{18}\text{O}/^{16}\text{O}$ ratio following the first dredge-up is related to metallicity. We note, however, that recent work by Leitner & Hoppe (2019); Verdier-Paoletti et al. (2019) and Hoppe et al. (2021) suggests that a portion of Group-1 and Group-2 (discussed below) presolar silicate grains may originate in SNe, intermediate-mass AGB stars, and super-AGB stars as determined by Mg-isotopic analyses consistent with such origins.

Group-2 grains are characterized by enrichments in ^{17}O and large depletions in ^{18}O relative to solar system values. Group-2 grains were attributed to origins in $< 2 M_{\odot}$ AGB stars (Boothroyd et

al. 1994; Nittler et al. 1997; Boothroyd & Sackmann 1999; Nollett et al. 2003). However, more recent nucleosynthetic models suggest that some grains could have origins in intermediate mass (4 to 8 M_{\odot}) AGB stars (Lugaro et al. 2017). The large ^{18}O depletions are not predicted by standard models and require an extra mixing process, which has been referred to as ‘cool-bottom processing’ or ‘hot bottom burning’ depending on whether the star is of low or intermediate mass, respectively. These mixing processes are used to explain the isotopic compositions observed in these grains (e.g., Wasserburg et al. 1995; Nollett et al. 2003; Lugaro et al. 2017). Such mixing destroys ^{18}O via the reaction $^{18}\text{O}(p, \alpha)^{15}\text{N}$ and therefore, the ^{18}O composition of Group-2 grains cannot be compared to model predictions to infer metallicity.

Group-4 grains are characterized by enrichments in ^{18}O and some have enrichments in ^{17}O above solar system values. These grains are thought to have condensed in the ejecta of type-II core-collapse SNe (Choi et al. 1998; Nittler et al. 2008). The enrichments in ^{18}O are thought to result from partial He burning in the He/C zone of massive stars via $^{14}\text{N}(\alpha, \gamma)^{18}\text{F}(e^+, \nu)^{18}\text{O}$. Some Group-4 grains that have ^{17}O compositions above solar composition that are suggested to follow the galactic chemical evolution trend and indicate a progenitor star with higher than solar metallicity. The Mg, Si, and Fe isotopic compositions of some Group-4 grains are not compatible with high metallicity stars, however, they are reproducible with nucleosynthetic models of SNe (Choi et al. 1998; Vollmer et al. 2008; Nittler et al. 2008; Nguyen & Messenger 2014a).

In addition to grains providing information on the nucleosynthetic processes of their progenitor stars, they can also help us constrain the conditions in which they condensed in their host circumstellar envelopes. Comparison of the chemical compositions and crystal structures of the grains to equilibrium and nonequilibrium thermodynamic model predictions (e.g., Gail & Sedlmayr 1999; Ebel & Grossman 2000; Ferrarotti & Gail 2001; Lodders, 2003) helps us to infer the temperatures at which mineral phases will condense from a gas, typically defined as solar composition or some variation thereof, under a presumed set of total pressures (e.g., Stroud et al. 2004; Vollmer et al. 2007, 2009, 2013; Zega et al. 2011, 2014, 2015; Nguyen et al. 2007, 2010, 2016). Solar composition can be a reasonable assumption for circumstellar environments, especially in grains whose isotopic composition indicates formation in a solar-metallicity star (e.g., Nittler et al. 2008; Lugaro et al. 2017). Regarding the pressures expected in circumstellar envelopes, we note that models of C stars estimate a range of pressures, with the photospheric region ranging from 10^{-3} to 10^{-5} bar and the envelope expected to have even lower pressures

(Lodders & Fegley 1995). Additionally, models of the circumstellar outflows of O-rich AGB stars estimate a range of pressures, between 10^{-10} to 10^{-6} bar (Gail & Sedlmayer 1999, Jeong et al. 2003). Therefore, comparison of the grain data to thermodynamic model predictions can provide first-order constraints on the thermodynamic conditions under which these grains condensed around their host stars.

Given the energetic nature of SNe environments (e.g., Arnett et al. 1989; Hughes et al. 2000), comparison of grain data with equilibrium thermodynamic models specific to the solar nebula could pose challenges. However, there are some models of dust condensation specific to SNe environments. For example, Fedkin et al. (2010) used model compositions of thin layers of ejecta within the main burning zones of type-II SNe computed by Rauscher et al. (2002) to predict the chemical compositions of minerals that condensed via equilibrium processes in 15-, 21- and 25 M_{\odot} SNe. There are also models that predict dust condensation via kinetic processes that take into account nucleation and grain growth (Todini & Ferrara 2001; Nozawa et al. 2003; Cherchneff & Dwek 2010) and can provide information such as the compositions of grains, their sizes, the zone of formation within the SN structure and the timescale of condensation following the SN explosion. We note that the grain sizes predicted by kinetic models of dust condensation in SNe are much smaller than those typically observed in the laboratory. Additionally, kinetic models show differences in condensation temperatures depending on how the time evolution of the gas temperature is calculated. For example, Todini & Ferrara (2001) use observational data from SN1987A in their calculations of the time evolution of gas temperature. Alternatively, Nozawa et al. (2003) calculate the evolution of the gas temperature using a multifrequency radiative transfer code together with the energy equation. Below we discuss the grain properties, how they compare to nucleosynthetic and thermodynamic models, and infer their origins.

Origins of AGB/RGB Grains

DOM-49

STEM images of DOM-49 do not reveal a distinct grain below the Pt fiducial marker that indicates the location of the O-anomalous region. While SAED patterns from the domain show that it is crystalline, we cannot pinpoint an individual grain that is the carrier of the O-anomaly and therefore we consider the domain shown (Fig. 2b-c) as the presolar ‘grain’. Comparing the O-isotope data with model predictions for AGB/RGB stars, DOM-49 is consistent with a close to

solar metallicity RGB or AGB star of roughly $1.3 M_{\odot}$ (Boothroyd et al. 1994; Boothroyd & Sackmann 1999). The olivine solid solution is predicted to condense via equilibrium processes at 1444 K and pure forsterite is expected at 1354 K assuming a total pressure of 10^{-3} and 10^{-4} bars respectively (Ebel & Grossman 2000; Lodders 2003). However, Fe-rich phases are not predicted to condense via equilibrium processes from a gas of solar composition (Ebel & Grossman 2000; Lodders 2003). Therefore, the nonstoichiometric and Fe-rich nature of DOM-49 suggests it could have formed via nonequilibrium processes.

Crystalline and amorphous olivine presolar grains from AGB stars were previously studied in meteorites and IDPs using TEM and are reported to contain varied amounts of Fe (Messenger et al. 2005; Busemann et al. 2009; Vollmer et al. 2009; Stroud et al. 2009, 2014; Nguyen et al. 2016; Nittler et al. 2018; Zega et al. 2020). The Fe contents of the amorphous grains are notably higher than the Fe contents in the crystalline grains. High Fe contents are consistent with models of nonequilibrium condensation, which show that amorphous olivine grains can contain higher Fe contents than crystalline olivine grains that formed through equilibrium condensation (Gail & Sedlmayr 1999; Ferrarotti & Gail 2001; Ebel & Grossman 2000; Lodders 2003). Additionally, astronomical observations of O-rich stars suggest Fe-rich olivine is more commonly amorphous than crystalline (Molster et al. 2002a, 2002b). Multiple scenarios were suggested to explain the incorporation of Fe into presolar crystalline olivine grains. One suggestion is that the olivine grain first formed as an amorphous grain with an Fe-rich composition and was later crystallized by thermal annealing processes in stellar wind (Nguyen et al. 2016). Alternatively, Messenger et al. (2005) suggested that higher Fe contents could be obtained if the olivine grain formed at high temperatures under oxidizing conditions, which would allow for a greater availability of FeO that could be incorporated into the olivine. Finally, these grains could have formed through nonequilibrium processes to obtain higher Fe contents, as mentioned above, or could incorporate Fe during parent body alteration.

The nonstoichiometric composition and crystalline structure of DOM-49 could suggest a scenario where the olivine grain formed first as an amorphous grain through nonequilibrium processes before being thermally annealed to a crystalline grain. Whether or not a single crystal would form from an amorphous grain would depend on its initial size and the availability of nucleation sites (Varshneya 1993, Callister & Rethwisch 2014). Alternatively, the higher Fe content could have been incorporated into the olivine at high temperatures under oxidizing

conditions where FeO is more abundant. Parent body alteration is also a possibility, but given that DOM 08006 experienced minimal alteration (Davidson et al. 2019), none of which is observed in the FIB section containing DOM-49, and that the Fe content is relatively homogeneous argues against parent-body alteration.

While we were not able to determine definitively the mineral phase of the Fe, Ni, S region given its small size, iron sulfides are predicted to condense at lower temperatures than silicate minerals such as olivine and pyroxene (Lodders 2003). Therefore, the presence of a low-temperature phase within a silicate grain suggests DOM-49 formed through a nonequilibrium process. Presolar silicates with iron sulfides were previously reported with compositions similar to glass with embedded metal and sulfides (GEMS, Messenger et al. 2003; Floss et al. 2006; Vollmer et al. 2009; Keller & Messenger 2011; Bradley et al. 2014). However, DOM-49 lacks nanocrystalline kamacite and pyrrhotite and the amorphous structure indicative of GEMS grains (Bradley 1994; Dai & Bradley 2001). Thus, a GEMS-like material can be ruled out.

As noted above, recent work by Leitner & Hoppe (2019), Verdier-Paoletti et al. (2019) and Hoppe et al. (2021) suggests that some Group-1 presolar silicate grains thought to originate in AGB/RGB stars could instead have condensed in SNe ejecta. While we do not have Mg isotopic data to confirm a SN origin, we discuss the possibility here. The nonstoichiometric, Fe-rich composition of DOM-49 suggests a kinetic origin. Kinetic models of dust condensation in SNe predict Mg-silicates to condense in SNe ejecta around 1400 to 1500 K (Nozawa et al. 2003) and also around 1100 K (Todini & Ferrara 2001). Fe-sulfides such as FeS are predicted to condense at lower temperatures of 1000 to 1100 K (Nozawa et al. 2003). The presence of a low-temperature Fe, Ni, S phase within the silicate would therefore be consistent with mixing in the SN ejecta, where transport and changing thermodynamic conditions led to the formation of the assemblage observed in DOM-49. Without further isotopic analyses, it is not possible to confirm whether an AGB/RGB or SN origin is more plausible for DOM-49. However, we note that only a small fraction (~3-12%) of Group-1 silicates are thought to have SN origins (Leitner & Hoppe 2019) and so the statistics would appear to favor an AGB/RGB origin.

DOM-59

STEM images reveal DOM-59 is a discrete presolar grain that conforms to forsterite structure and chemistry. Comparison of the O-isotopic composition of DOM-59 with model predictions is

consistent with an origin in an AGB star of roughly $1.65 M_{\odot}$ (Boothroyd et al. 1994; Boothroyd & Sackmann 1999). While we cannot confirm the metallicity of the progenitor star of Group-2 grains, we note that solar composition was used to reproduce the trends defined by Group-2 grains to understand their origins in AGB stars (e.g., Nittler et al. 2008; Lugaro et al. 2017).

Comparison of grain data with equilibrium thermodynamic model predictions provides constraints on the origin of DOM-59. The TEM data show that DOM-59 is an olivine, both structurally (Fig. 4h) and compositionally within error (Fig. 4g). The olivine solid solution is predicted to condense from a cooling gas of solar composition at 1444 K and 1240 K assuming total pressures of 10^{-3} and 10^{-6} bars respectively (Ebel & Grossman 2000). The spatial relationships that we observe in DOM-59 are consistent with solids sequentially condensing out of a monotonic cooling gas of solar composition. The microstructure observed for DOM-59 is therefore consistent with the Ca-rich core having condensed first, followed by the Mg-rich shell in order to produce the core-shell structure we observe in DOM-59.

As mentioned above for DOM-49, previous studies have reported presolar olivine grains from diverse stellar origins including AGB/RGB stars and supernovae (Messenger et al. 2005; Busemann et al. 2009; Vollmer et al. 2009; Stroud et al. 2009, 2014; Nguyen et al. 2016; Nittler et al. 2018; Zega et al. 2020). These studies include both crystalline and amorphous grains, some of which conform to equilibrium condensation and some that likely formed through nonequilibrium processes. Core-mantle structures similar to what we observe here for DOM-59 were reported in the literature, including a spinel grain surrounded by Mg-rich silicate (Nguyen et al. 2014b), where the spinel core is thought to have formed through equilibrium processes, while the mantle suggests nonequilibrium formation. An Al-Ca-Ti oxide surrounded by a Ca-rich silicate was also reported but no TEM data are available, leaving its origins ambiguous (Leitner et al. 2018). Recently, two grains with core-mantle structures were reported in DOM 08006 (Nittler et al. 2018; Zega et al. 2020). First, a Ca-Al-rich core surrounded by ferromagnesian silicates was reported (DOM-77, Nittler et al. 2018) and is consistent with equilibrium condensation. Finally, a presolar spinel grain surrounded by solar Mg-silicate was observed (DOM-9, Zega et al. 2020) and is consistent with nonequilibrium condensation. We discuss the implications of the Fe-rich rim that surrounds DOM-59 below.

Fe-rich rims around oxide and silicate presolar grains were previously reported in the Adelaide, Acfer 094 and QUE 99177 meteorites (Vollmer et al. 2009; Floss & Stadermann 2012; Nguyen et

al. 2016; Zega et al. 2020). Vollmer et al. (2009) reported an olivine grain in Acfer 094 with an amorphous Fe-rich rim that was suggested to have formed through amorphization due to sputtering in the ISM. Nguyen et al. (2016) reported an enstatite grain in QUE 99177 with an amorphous Fe-silicate rim and suggested formation through parent-body alteration. The Fe-rims from Acfer 094 and QUE 99177 differ from DOM-59 in that they do not have a compositional gradient. Floss and Stadermann (2012) identified two silicate grains with Fe-rims in the Adelaide meteorite consistent with Fe-diffusion resulting from secondary processes possibly due to short-lived thermal processing of mm- to cm-sized clumps of dust in an oxidizing nebular environment with elevated gas-to-dust ratios. Similarly, TEM analyses by Zega et al. (2020) suggest that Fe-rich rims and heterogenous distributions of Fe throughout the matrix are indicators of thermal processing of fragments of dust. Such secondary alteration in the solar nebula resulted in material that was processed to varied degrees and incorporated into the Adelaide matrix. Compared to these previously identified Fe-rich rims in silicate and oxide presolar grains, the chemically zoned and diffusion-like structure of the rim around DOM-59 (Fig. 4c) is most similar to those observed in the Adelaide meteorite. However, we note that the Adelaide meteorite has experienced significantly more alteration and has a smaller abundance of O-rich presolar grains compared to DOM 08006 (Floss & Stadermann 2012; Haenecour et al. 2018; Nittler et al. 2018; Davidson et al. 2019). In any case, Fe-rich rims around presolar grains and solar-system derived grains within the matrices of their host meteorites are generally regarded as a signature of thermal processing. Whether the rim in DOM-59 formed through such processing is worth exploring.

DOM 08006 was reported to be the most primitive CO chondrite, with very minor evidence for parent body aqueous alteration and terrestrial weathering (Davidson et al. 2019). Such evidence includes metal being altered to magnetite and Fe oxyhydride needles, which are not observed here (Davidson et al. 2019). The matrix of other FIB sections in this study do not contain phases characteristic of parent-body alteration, which argues against parent-body processing as having formed the Fe-rich rim around DOM-59. Thus, the origin of the Fe-rich rim more likely involved processing that was pre-accretionary in the solar nebula or host circumstellar envelope.

One other possible formation pathway for the Fe-rim in DOM-59 includes condensation of the Fe-rim around the compositionally zoned olivine grain. Presolar Fe-bearing oxides were previously identified (Floss et al. 2008; Bose et al. 2010a; Zega et al. 2015; Haenecour et al. 2018), and are predicted to condense at lower temperatures than the olivine solid solution (e.g., Ebel &

Grossman 2000). Thus, it is conceivable that an olivine grain could provide a nucleation site for the Fe-rich rim to condense. Condensation of the rim via equilibrium processes would likely produce a homogeneous distribution of Fe around DOM-59. We note that because a portion of the grain was milled through during the final thinning of the FIB section, we do not know if the Fe-rim originally surrounded the entirety of DOM-59. Given that we also observe Fe-rich veins throughout the FIB section containing DOM-59, we infer that the Fe-rich rim around DOM-59 and the surrounding matrix represent a clump of dust that was altered in the solar nebula in an environment similar to that described by Floss and Stadermann (2012). The lack of Fe-rich rims in the other FIB sections in this study suggests that the alteration may have been inherited by the material accreted onto the parent body asteroid.

As noted above, recent work by Leitner & Hoppe (2019), Verdier-Paoletti et al. (2019) and Hoppe et al. (2021) suggests that a fraction of Group-2 presolar silicate grains could originate in SNe. We do not have Mg isotopic data for DOM-59 to confirm such an origin, but we discuss the possibility here. Equilibrium models of dust condensation of SNe predict olivine to condense between 1576 and 1063 K. Thus, if DOM-59 formed in SN ejecta and the core-mantle structure observed is consistent with equilibrium condensation, the Ca-core likely condensed first, followed by the Mg-rich mantle at lower temperatures. The Fe-rich rim is consistent with nebular origins as discussed above.

Origins of SN Grains

DOM-22

The polycrystalline region of DOM-22 has d-spacings common to both olivine and pyroxene (Table 2), and precludes the identification of a single grain that is the carrier of the isotopic anomaly. To ensure that we correctly located and marked the O-anomalous region DOM-22, we verified the location of DOM-22 by further correlating images from the NanoSIMS to those in the FIB-SEM prior to sectioning. Therefore, we consider the polycrystalline domain shown (Fig. 5b-d) as the presolar ‘grain’. Given the Fe-rich composition of DOM-22 and the presence of Fe-sulfides in the polycrystalline domain, it is difficult to reconcile this microstructure with equilibrium predictions.

Polycrystalline and amorphous presolar silicate grains were identified within meteoritic samples (Stroud et al. 2009; Vollmer et al. 2009; Nguyen et al. 2010; Zega et al. 2020). Stroud et

al. (2009) reported forsterite-like nanocrystalline and amorphous material with a nonstoichiometric composition and inferred formation under nonequilibrium conditions. Vollmer et al. (2009) identified a cluster of several amorphous, nonstoichiometric silicate particles that are similar to GEMS and are thought to have formed through nonequilibrium condensation. Nguyen et al. (2010) reported several amorphous grains with nonstoichiometric compositions and suggested the grains could have formed through multistep or nonequilibrium condensation. Zega et al. (2020) identified a polycrystalline assemblage of ferromagnesian silicates that could have formed through multistep condensation followed by mechanical accretion in the host circumstellar envelope. In comparison, the Fe-rich polycrystalline assemblage and nonstoichiometric pentlandite grain of DOM-22 is not consistent with equilibrium condensation. We therefore infer that DOM-22 formed through nonequilibrium or multistep condensation, the details of which will be discussed below.

The ejecta of SNe are dynamic environments and individual grains formed within them have the ability to record snapshots of the likely rapidly changing conditions within SNe. Astronomical observations of SN remnants displaying heterogeneous compositions and clumpy structures suggest that large-scale mixing likely occurs in their ejecta, which is supported by both the isotopic compositions of SN grains and modeling efforts that describe how such mixing occurs (Arnett et al. 1989; Hughes et al. 2000; Kifonidis et al. 2003; Hammer et al. 2010; Abarzhi et al. 2019). Kinetic models of SN ejecta predict Mg-rich silicates to condense between 1400 to 1500 K (Nozawa et al. 2003), and around 1100 K (Todini & Ferrara 2001). Both equilibrium and kinetic models predict iron sulfides to condense at lower temperatures (704 K, Lodders 2003; 1000-1100 K, Nozawa et al. 2003) than those suggested for Mg-silicates. Therefore, we consider two possible scenarios for the formation of DOM-22. First, as temperatures cooled in the host SN ejecta, the polycrystalline assemblage could have formed in a stepwise manner, with the ferromagnesian silicate condensing first, followed by the Fe-sulfides at lower temperatures which were then mechanically accreted together with the silicate. Alternatively, the Fe-sulfides condensed first in a cooler region of the SN ejecta and was then transported to a warmer region where the polycrystalline ferromagnesian silicate could condense around it. Given the structure observed in DOM-22, it is difficult to distinguish between these two scenarios and it is also unclear whether the Fe-sulfides contained within the polycrystalline domain are in fact presolar in origin. If the Fe-sulfides are not presolar in origin, they likely formed in the early solar system or in the ISM before

being mechanically accreted to the presolar ferromagnesian silicate assemblage either as free-floating objects or on the parent body asteroid. These observations therefore preclude constraining the precise conditions under which it formed. However, a nonequilibrium, multistep formation mechanism is likely.

DOM-35

Equilibrium condensation of forsterite is predicted by Fedkin et al. (2010) in a 15 to 25 M_{\odot} SN between 1063 and 1575 K. Thus, the single crystal forsterite on the left side of DOM-35 is consistent with equilibrium condensation. Fedkin et al. (2010) notes that in the H and He/N zones of the ejecta, the olivine equilibrium mole fraction (X_{Fa}) is <0.002 above 1000 K, whereas forsterite that occurs in the O-rich zones between 1500 K and 1600 K has $X_{Fa}<0.03$. The polycrystalline portion of DOM-35 is more Fe-rich than the single crystal forsterite, with $X_{Fa}>0.03$. Fedkin et al. (2010) note that to produce more Fe-rich olivine compositions ($X_{Fa}>0.03$) via equilibrium processes in SN dust, mixing is required between different SN layers. It is therefore possible that the polycrystalline portion of DOM-35 condensed via equilibrium processes. As noted above, large-scale mixing likely occurs in the ejecta of SNe and the microstructures observed in DOM-35 are consistent with the single crystal and polycrystalline forsterite being brought together through large-scale mixing processes.

One other SN olivine aggregate ‘B10A’, was identified in an interplanetary dust particle (IDP) and was suggested to have condensed via equilibrium processes in a 15 M_{\odot} SN at 1560 K in a solar metallicity star (Messenger et al. 2005). Similar to DOM-35, B10A also has an Fe-rich composition that required mixing to produce its composition, however its isotopic composition is significantly different. While it is possible that DOM-35 formed under similar thermodynamic conditions to B10A, the difference in isotopic composition suggests different nucleosynthetic origins.

DOM-39

The orthopyroxene solid solution is predicted to condense via equilibrium processes in a 15 to 25 M_{\odot} SN between 1090 to 1548 K (Fedkin et al. 2010). However, the Fe-sulfide and orthopyroxene assemblage observed in DOM-39 is difficult to reconcile with monotonic equilibrium cooling. While the orthopyroxene solid solution is not considered in available kinetic models of dust condensation (Todini and Ferrara 2001; Nozawa et al. 2003), pyroxenes have been

observed in the Cas A SN remnant (Rho et al. 2009). Kinetic models do consider the pure endmember enstatite, which is suggested to condense between 1400 to 1500 K (Nozawa et al. 2003) and at 1100 K (Todini & Ferrara 2001). Below we explore formation scenarios for both presolar and solar origins of the iron sulfide and the surrounding orthopyroxene.

It is difficult to explain the microstructure observed in DOM-39 without both the Fe-sulfide and the orthopyroxene having presolar origins. A solar origin would require the mechanical accretion of an Fe-sulfide that contains an Fe-oxide rim with the presolar orthopyroxene. In this scenario, the Fe-sulfide would have accreted to the outside of the orthopyroxene, which is not what we observe (Fig. 7e). Alternatively, the presolar orthopyroxene could have provided a nucleation site for Fe-sulfide formation in the solar protoplanetary disk. However, the continuous rim that surrounds the Fe-sulfide (Fig. 7c-d; supplementary Fig. 13) but not the orthopyroxene is not consistent with this scenario.

Fe-sulfides are more volatile than pyroxenes and therefore are predicted to condense at lower temperatures (e.g. ~ 1000 K) than Mg-rich pyroxenes (e.g. 1400-1500 K, Nozawa et al. 2003) through both equilibrium and kinetic processes. However, the nonstoichiometric composition of the Fe-sulfide in DOM-39 is inconsistent with equilibrium predictions, and so condensation via kinetic processes seems more realistic. That the Fe-sulfide grain has a continuous oxide rim but its host orthopyroxene does not suggests that the former formed before the latter. We hypothesize that the continuous rim on the Fe-sulfide was acquired as it was a freely floating object in the ejecta under oxidizing conditions before becoming embedded within the orthopyroxene. This scenario would imply that the embedded Fe-sulfide within the orthopyroxene in DOM-39 is also presolar in origin.

As mentioned above for DOM-22, the conditions within the ejecta of SNe are likely rapidly changing and large-scale mixing is likely occurring. One possible formation scenario for the DOM-39 assemblage is that after acquiring its rim, the Fe-sulfide was transported to a region of the ejecta where conditions were favorable for orthopyroxene to condense around the Fe-sulfide. Alternatively, the entire DOM-39 assemblage could have formed through a nonequilibrium process where the Fe-sulfide and rim formed and subsequently provided a nucleation site for the orthopyroxene to condense. We note that TEM studies on two other SN pyroxene grains were reported in the literature, both of which are amorphous. One of these grains is stoichiometric

enstatite, which is consistent with equilibrium condensation followed by amorphization. The second grain is nonstoichiometric with a high-Ca pyroxene composition (Nguyen et al. 2016).

DOM-50

The polycrystalline domain of DOM-50 suggests a multiphase carrier of the isotope anomaly. The anomaly was still present in the last NanoSIMS raster ion image and DOM-50 was carefully located and marked by correlating images from the NanoSIMS and FIB-SEM. We are therefore confident that the entire polycrystalline domain is the anomalous presolar ‘grain’. As noted above with DOM-35, more Fe-rich compositions are possible via equilibrium condensation in SNe if there is large-scale mixing in the ejecta (Fedkin et al. 2010). However, the Fe content of DOM-50 exceeds the Fe content required for stoichiometric Fe-rich endmembers of both olivine and pyroxene and therefore cannot be explained by mixing in the SN ejecta in conjunction with equilibrium condensation. Thus, DOM-50 likely formed through nonequilibrium processes in its host SN ejecta. While Fe-rich silicates were previously reported in presolar silicate grains from AGB/RGB origins, Nguyen et al. (2016) reported the only other TEM analysis of an Fe-rich SN silicate to date. The grain, 2_33b, is a GEMS-like Fe-rich silicate and differs from DOM-50 in that it is both nonstoichiometric and amorphous, which is suggestive of formation through nonequilibrium processes.

Previous studies have discussed the origins of Fe in presolar silicate grains (Nguyen et al. 2007, 2010; Floss & Stadermann 2009a; Vollmer et al. 2009; Bose et al. 2010a; Ong & Floss 2015). In altered meteorites, secondary processing plays a role in the origin of Fe in presolar silicates (Ong & Floss 2015). However, in pristine meteorites with a high abundance of presolar grains, such as DOM 08006, the Fe is likely primary (Ong & Floss 2015). Fe-isotopic analyses of Group-4 presolar silicate grains are consistent with the primary origin of Fe in SN silicates (Ong & Floss 2015). The SN silicates analyzed contain $^{54}\text{Fe}/^{56}\text{Fe}$ and $^{57}\text{Fe}/^{56}\text{Fe}$ ratios consistent with formation in the outer zones of type-II core collapse SNe (Ong & Floss 2015). We hypothesize that the Fe-rich compositions of both DOM-22 and DOM-50 reported above are primary in origin.

Presolar Grain Constraints on Dust Composition/Formation in SN Ejecta

To date, more than 1,500 O-rich presolar grains have been identified with stellar origins including RGB, AGB stars, novae, and SNe (e.g., Nittler et al. 1994, 1997, 1998, 2008, 2018; Huss

et al. 1994; Choi et al. 1998, 1999; Zinner et al. 2003, 2005; Messenger et al. 2003, 2005; Mostefaoui & Hoppe 2004; Nagashima et al. 2004; Nguyen & Zinner 2004; Tonotani et al. 2006; Ebata et al. 2006; Floss et al. 2006, 2010, 2013; Nguyen et al. 2007, 2010, 2014a; Busemann et al. 2009; Floss & Stadermann 2009a, 2009b, 2012; Vollmer et al. 2009; Gyngard et al. 2010a, 2010b; Bose et al. 2010, 2012, 2014; Zhao et al. 2010, 2011, 2013; Keller & Messenger 2011; Leitner et al. 2012a, 2014, 2016, 2020; Davidson et al. 2012, 2014, 2015; Haenecour et al. 2013, 2018, 2019, 2020). Of the grains identified in meteorites, only ~10% are attributed to origins in the ejecta of SNe (Haenecour et al. 2018), though as previously mentioned, recent nucleosynthetic modeling suggests this fraction could be much higher, as some Group-1 and Group-2 presolar silicate grains could originate in SNe (Leitner & Hoppe 2019; Verdier-Paoletti et al. 2019; Hoppe et al. 2021). Similarly, the fraction of SN grains is also higher if smaller grain sizes are considered (Hoppe et al. 2015). Nonetheless, detailed analyses of the structure and chemistry of grains derived from SNe are severely limited, with only fourteen O-rich grains (including this work) analyzed using TEM (Messenger et al. 2005; Floss et al. 2006; Zega et al. 2011; Keller & Messenger 2011; Takigawa et al. 2014; Nguyen et al. 2016, 2017).

Previous studies reveal that SN silicates have ferromagnesian compositions and both stoichiometric and nonstoichiometric compositions are reported. Additionally, both amorphous and crystalline structures were reported, with amorphous structures appearing to be higher in abundance (~70%, Nguyen et al. 2016). The SN silicates that we have discussed here are consistent with the previously reported grain diversity in chemistry, including olivine, pyroxene, and intermediate phases, but differ from previous studies in that they all have crystalline structures (either single crystal or polycrystalline) and are more Fe-rich. In comparison, astronomical observations suggest a greater abundance of amorphous silicates with MgSiO_3 and Mg_2SiO_4 compositions in the ejecta of SNe (e.g., Arendt et al. 1999; Rho et al. 2008, 2009). However, astronomical observations do bear some uncertainty, as it can be difficult to distinguish dust formed in the SN ejecta and the ISM. Based on the limited statistics, it is unclear whether there is a bias in the grain data because of the small number of detailed studies on SN silicates or if Fe-rich crystalline silicates in SNe are preferentially preserved and therefore more abundant than previously suggested. As noted above, the Fe-bearing compositions of presolar silicates in unaltered meteorites are likely primary features (Ong & Floss 2015), which would appear to argue against a bias in the grain data. Additionally, two of the SN silicates we discuss contain iron sulfide

inclusions that appear to be contained within the isotopically anomalous regions of interest and would represent the first observations of iron sulfides from a SN origin. To date, two other iron sulfides that are not GEMS-like were observed within a presolar silicate and a graphite grain from AGB stars (Haenecour et al. 2016, 2020). Astronomical observations do suggest the presence of iron sulfides such as FeS in circumstellar environments and the ejecta of SNe (e.g., Hony et al. 2003; Rho et al. 2008). Additionally, work by Köhler et al. (2014) suggests that FeS nano-inclusions in amorphous silicates could provide a reservoir for S in the ISM. Iron sulfides such as FeS are predicted in equilibrium models of dust condensation in a solar composition gas (e.g., Lodders 2003) and in kinetic models of dust condensation in SNe (Nozawa et al. 2003). Iron sulfides were common in the solar protoplanetary disk based on the meteoritic record (Lauretta et al. 1996, 1997, 1998; Scott & Krot 2014) and the CSE of a solar-composition star might be expected to form FeS if it experiences equilibrium or kinetic condensation. In short, we might expect presolar sulfides to occur in CSEs of solar-metallicity stars in the galaxy. However, why a single crystal of presolar troilite or pyrrhotite has not been identified to date is unclear, but we suspect it could be related to the ability of sulfide materials to survive ISM transport and solar-system formation (Heck et al. 2012; Hoppe et al. 2012; Zhao et al. 2013). To date, that the only candidate presolar Fe-sulfide grains identified are present as small inclusions inside of other presolar grains would appear to be consistent with sulfides having a higher susceptibility to processing and destruction than other types of presolar grains (Haenecour et al. 2016). A higher susceptibility to processing is supported by previous laboratory work that suggests FeS grains produced around evolved stars and injected into the ISM will be destroyed more quickly than crystalline silicate grains (Keller & Rahman 2011). It remains to be seen whether single-crystal presolar sulfide grains will be identified in future presolar-grain studies.

Comparing the analyses of SN silicates with previous studies from AGB/RGB origins reveals similarities in the variety of mineralogies and structures observed. Including this work, of the SN silicates analyzed using TEM, half are amorphous and half are crystalline (single crystal or polycrystalline, Messenger et al. 2005; Floss et al. 2006; Nguyen et al. 2016). Similarly, TEM analyses of AGB/RGB silicates show comparable distributions of amorphous and crystalline grains, with about 46% of grains being amorphous, about 44% being crystalline (single crystal or polycrystalline), and the remainder are composite grains (Messenger et al. 2003; Vollmer et al. 2007, 2009, 2013; Nguyen et al. 2007, 2010, 2013, 2014a, 2016; Busemann et al. 2009; Floss &

Stadermann 2009a; Keller & Messenger 2011; Stroud et al. 2013, 2014; Haenecour et al. 2020; Nittler et al. 2020; Zega et al. 2020). Additionally, both stellar sources show evidence for equilibrium and nonequilibrium formation processes. As with previous TEM studies of presolar grains from AGB/RGB stars and SNe, it does not appear that there are significant differences in silicate grains derived from the different stellar origins, which suggests that the circumstellar envelopes of AGB/RGB stars and the ejecta of SNe can have similar local thermodynamic landscapes.

Conclusions

This work reports detailed chemical and mineralogical analyses of six presolar silicate grains from the CO3.0 carbonaceous chondrite DOM 08006. O-isotopic compositions of two of the grains are consistent with formation in the circumstellar envelopes of evolved AGB/RGB stars and the remaining four grains are consistent with origins in the ejecta of type-II core collapse SNe. TEM data reveal that all of the analyzed grains are crystalline. One of the AGB grains is a Fe-rich olivine with an Fe-Ni sulfide inclusion that likely formed under nonequilibrium conditions around a low-mass ($\sim 1.3M_{\odot}$) star with close to solar metallicity. The second AGB grain is a chemically zoned olivine grain that contains a Ca-rich core, Mg-rich shell, and an Fe-oxide rich rim. The core-shell structure is consistent with equilibrium condensation from a cooling gas of solar composition in a low-mass ($\sim 1.65M_{\odot}$) AGB star with the Ca-rich core and Mg-rich shell condensing sequentially. We infer that the Fe-rich rim formed through nebular processing in an oxidizing environment, but a nonequilibrium process cannot be ruled out. Two of the SN grains are polycrystalline and have compositions consistent with a mixture of olivine and pyroxene and likely formed through nonequilibrium processes. The third SN grain contains both single crystal and polycrystalline forsterite that were likely brought together through large-scale mixing processes and formed between 1063 K and 1575 K in a 15 to 25 M_{\odot} SN. The fourth SN grain is a crystalline orthopyroxene grain with an embedded Fe-sulfide that appears to be contained within the anomalous hotspot. This observation would, to our knowledge, be the first report of a presolar Fe-sulfide within a SN silicate grain. Given that the Fe-sulfide contains a complete rim, it must have formed before incorporation into the surrounding orthopyroxene, which suggests transport in the SN ejecta and is not consistent with monotonic equilibrium cooling. Despite the differences between circumstellar shells of AGB/RGB stars and the ejecta of SNe, our examination of these

preserved stardust grains suggests that each of these distinct astrophysical environments can condense similar types of dust with comparable structures and compositions.

Acknowledgements

We gratefully acknowledge the late Professor Christine Floss for her contributions to the identification of the grains analyzed here through NASA grant NNX14AG25G. The research completed here was supported by NASA grants NNX15AJ22G and 80NSSC19K0509. We also acknowledge NASA grants NNX12AL47G, NNX15AJ22G, 80NSSC19K0509, and NSF grant 1531243 for funding instrumentation in the Kuiper Materials Imaging and Characterization Facility at LPL. We thank Tarunika Ramprasad for helpful questions and conversations provided towards the data interpretation and manuscript. We thank Jan Leitner, Christian Vollmer, and an anonymous reviewer for constructive reviews that greatly improved the manuscript.

References

- Abarzhi S., Bhowmick A. K., Naveh A., Pandian A., Swisher N. C., Stellingwerf R. F. and Arnett W.D. 2019. Supernova, nucleosynthesis, fluid instabilities, and interfacial mixing. *Proceedings of the National Academy of Science* 116:18184-18192.
- Amari S., Hoppe P., Zinner E. and Lewis R. S. 1992. Interstellar SiC with unusual isotopic compositions: Grains from a supernova? *The Astrophysical Journal* 394:L43-46.
- Amari S., Zinner E. and Lewis R. S. 1995. ^{41}Ca in circumstellar graphite from supernovae. *Meteoritics* 30:480.
- Arendt R. G., Dwek E. and Moseley S. H. 1999. Newly synthesized elements and pristine dust in the Cassiopeia A supernova remnant. *The Astrophysical Journal* 521:234-245.
- Arendt R. G., Dwek E., Kober G., Rho J. and Hwang U. 2014. Interstellar and ejecta dust in the Cas A supernova remnant. *The Astrophysical Journal* 786:55.
- Arnett W. D., Bahcall J. N., Kirshner R. P. and Woosley S. E. 1989. Supernova 1987A. *Annual Reviews of Astronomy and Astrophysics* 27:629-700.
- Besmehn A. and Hoppe P. 2003. A nanoSIMS study of Si- and Ca-Ti-isotopic compositions of presolar silicon carbide grains from supernovae. *Geochimica et Cosmochimica Acta* 67:4693-4703.

- Boothroyd A. I., Sackmann I. -J. and Wasserburg G. J. 1994. Predictions of oxygen isotope ratios in stars and of oxygen-rich interstellar grains in meteorites. *The Astrophysical Journal* 430: L77-84.
- Boothroyd A. I. and Sackmann I. -J. 1999. The CNO-isotopes: Deep circulation in red giants and first and second dredge-up. *The Astrophysical Journal* 510:232-250.
- Bose M., Floss C. and Stadermann F. 2010a. An investigation into the Fe-rich presolar silicates in Acfer 094. *The Astrophysical Journal* 714:1624-1636.
- Bose, M. Floss C., Stadermann F., Stroud R. M. and Speck A. K. 2012. Circumstellar and interstellar material in the CO3 chondrite ALHA77307: An isotopic and elemental investigation. *Geochimica et Cosmochimica Acta* 93:77-101.
- Bose M., Zega T. J. and Williams P. 2014. Assessment of alteration processes on circumstellar and interstellar grains in Queen Alexandra Range 97416. *Earth and Planetary Science Letters* 399:128-138.
- Bradley J. P. 1994. Chemically anomolous preaccretionally irradiated grains in interplanetary dust from comets. *Science* 265:925-929.
- Bradley J. P. 2014. Early solar nebula grains—Interplanetary dust particles. In *Treatise on geochemistry volume 1: Meteorites and cosmochemical processes*, edited by Davis A. M. Amsterdam. Elsevier Ltd. pp. 287–308.
- Busemann H., Nguyen A. N., Cody G. D., Hoppe P., Kilcoyne A. L. D., Stroud R. M., Zega T. J. and Nittler L. R. 2009. Ultra-primitive interplanetary dust particles from the comet 26P/Grigg-Skjellerup dust stream collection. *Earth and Planetary Science Letters* 288:44-57.
- Busso M., Gallino R. and Wasserburg G. J. 2003. Short-lived nuclei in the early solar system: A low mass stellar source? *Publications of the Astronomical Society of Australia* 20:356-370.
- Callister W. D. and Rethwisch D. G. 2014. *Materials Science and Engineering: An Introduction*. Wiley.
- Cameron A. G. W. and Truran J. W. 1977. The supernovae trigger for formation of the solar system. *Icarus* 30:447-461.
- Cherchneff I. and Dwek E. 2010. The chemistry of population III supernova ejecta. II. the nucleation of molecular clusters as a diagnostic for dust in the early universe. *The Astrophysical Journal* 713:1-24.
- Choi B. G., Huss G. R. and Wasserburg G. J. 1998. Presolar corundum and spinel in ordinary

- chondrites: Origins from AGB stars and a supernova. *Science* 282:1282-1289.
- Choi B. G., Wasserburg G. J. and Huss G. R. 1999. Circumstellar hibonite and corundum and nucleosynthesis in asymptotic giant branch stars. *The Astrophysical Journal* 522:L133-136.
- Cliff G. and Lorimer G. W. 1975. The quantitative analysis of thin specimens. *Journal of Microscopy* 103:203-207.
- Dai Z. R. and Bradley J. P. 2001. Iron-nickel sulfides in anhydrous interplanetary dust particles. *Geochimica et Cosmochimica Acta* 65:3601-3612.
- Davidson J., Busemann H. and Franchi I.A. 2012. A NanoSIMS and Raman spectroscopic comparison of interplanetary dust particles from comet Grigg-Skjellerup and non-Grigg Skjellerup collections. *Meteoritics & Planetary Science* 47:1748-1771.
- Davidson J., Schrader D. L., Alexander C. M. O'D., Lauretta D. S., Busemann H., Domanik K. J. and Verchovsky A. 2014. Petrography, stable isotope compositions, microRaman spectroscopy, and presolar components of Roberts Massif 04133: A reduced CV3 carbonaceous chondrite. *Meteoritics & Planetary Science* 49:2133-2151.
- Davidson J., Nittler L. R., Stroud R. M., Takigawa A., Gregorio B. T. D. and Cody G. D. 2015. Organic matter in the unique carbonaceous chondrite Miller Range 07687: A coordinated in situ NanoSIMS, FIB-TEM, and XANES study (abstract #1609). 46th Lunar and Planetary Science Conference.
- Davidson J., Alexander C. M. O'D., Stroud R., Busemann H. and Nittler L. R. 2019. Mineralogy and petrology of Dominion Range 08006: A very primitive CO3 carbonaceous chondrite. *Geochimica et Cosmochimica Acta* 265:259-278.
- Ebata S., Nagashima K., Itoh S., Kobayashi S., Sakamoto N., Fagan T. J. and Yurimoto H. 2006. Presolar silicate grains in enstatite chondrites (abstract #1619). 37th Lunar and Planetary Science Conference.
- Ebel D. S. and Grossman L. 2000. Condensation in dust-enriched systems. *Geochimica et Cosmochimica Acta* 64:339-366.
- Fedkin A. V., Meyer B. S. and Grossman L. 2010. Condensation and mixing in supernova ejecta. *Geochimica et Cosmochimica Acta* 74:3642-3658.
- Ferrarotti A. S. and Gail H. P. 2001. Mineral formation in stellar winds II. Effects of Mg/Si abundance variations on dust composition in AGB stars. *Astronomy & Astrophysics* 371:133-151.
- Floss C., Stadermann F. J., Bradley J. P., Dai Z. R., Bajt S., Graham G. and Lea A. S. 2006. Identification of isotopically primitive interplanetary dust particles: A NanoSIMS isotopic imaging study. *Geochimica et Cosmochimica Acta* 70:2371-2399.

- Floss C., Stadermann F. J., and Bose M. 2008. Circumstellar Fe oxide from the Acfer 094 carbonaceous chondrite. *The Astrophysical Journal* 672:1266–1271.
- Floss C. and Stadermann F. 2009a. Auger nanoprobe analysis of presolar ferromagnesian silicate grains from primitive CR chondrites QUE 99177 and MET 00426. *Geochimica et Cosmochimica Acta* 73:2415-2440.
- Floss C. and Stadermann F.J. 2009b. High abundances of circumstellar and interstellar C-anomalous phases in the primitive CR3 chondrites QUE 99177 and MET 00426. *The Astrophysical Journal* 697:1242-1255.
- Floss C., Stadermann F. J., Mertz A. F. and Bernatowicz T. 2010. A NanoSIMS and auger nanoprobe investigation of an isotopically primitive interplanetary dust particle from the 55P/Tempel-Tuttle targeted stratospheric dust collector. *Meteoritics & Planetary Science* 45:1889-1905.
- Floss C. and Stadermann F. 2012. Presolar silicate and oxide abundances and compositions in the ungrouped carbonaceous chondrite Adelaide and the K chondrite Kakangari: The effects of secondary processing. *Meteoritics & Planetary Science* 47:992-1009.
- Floss C., Stadermann F.J., Kearsley A.T., Burchell M.J. and Ong W.J. 2013. The abundance of presolar grains in comet 81P/Wild 2. *The Astrophysical Journal* 763:140.
- Floss C. and Haenecour P. 2016. Presolar silicate grains: Abundances, isotopic and elemental compositions, and the effects of secondary processing. *Geochemical Journal* 50:3-25.
- Gail H. P. and Sedlmayr E. 1999. Mineral formation in stellar winds. I. Condensation sequence of silicate and iron grains in stationary oxygen rich outflows. *Astronomy & Astrophysics* 347:594-616.
- Gyngard F., Nittler L.R., Zinner E. and Jose J. 2010a. Oxygen-rich stardust grains from novae. *Proceedings of The 11th Symposium on Nuclei in the Cosmos*.
- Gyngard F., Zinner E., Nittler L.R., Morgand A., Stadermann F.J. and Hynes K.M. 2010b. Automated NanoSIMS measurements of spinel stardust from the Murray meteorite. *The Astrophysical Journal* 717:107-120.
- Haenecour P., Zhao X., Floss, C., Lin Y., Zinner E. 2013. First laboratory observation of silica grains from core collapse supernovae. *The Astrophysical Journal* 768:L17.
- Haenecour P., Floss C., José J., Amari S., Lodders K., Jadhav M., Wang A. and Gyngard F. 2016. Coordinated analysis of two graphite grains in the CO3.0 LAP 031117 meteorite: first identification of a CO nova graphite and a presolar iron sulfide subgrain. *The Astrophysical Journal* 825:88.

- Haenecour P., Floss C., Zega T. J., Croat T. K., Wang A., Jolliff B. L. and Carpenter P. 2018. Presolar silicates in the matrix and fine-grained rims around chondrules in primitive CO3.0 chondrites: Evidence for pre-accretionary aqueous alteration of the rims in the solar nebula. *Geochemical et Cosmochimica Acta* 221:379-405.
- Haenecour P., Howe J. Y., Zega T. J., Amari S., Lodders K., José J., Kaji K., Sunaoshi T. and Muto, A. 2019. Laboratory evidence for co-condensed oxygen- and carbon-rich meteoritic stardust from nova outbursts. *Nature Astronomy* 3:626-630.
- Haenecour P., Floss C., Brearley A. and Zega T. 2020. The effects of secondary processing in the unique carbonaceous chondrite Miller Range 07687. *Meteoritics & Planetary Science* 55:1228-1256.
- Hammer N. J., Janka H. -T. and Muller E. 2010. Three dimensional simulations of mixing instabilities in supernova explosions. *The Astrophysical Journal* 714:1371-1385.
- Heck P. R., Hoppe P., Huth J. 2012 Sulfur four isotope NanoSIMS analysis of Comet-81P/Wild 2 dust in impact craters on aluminum foil C2037N from NASA's Stardust mission. *Meteoritics & Planetary Science* 47: 649-659.
- Holzappel C., Soldera F., Vollmer C., Hoppe P., Mucklich F. 2009. TEM foil preparation of sub-micrometer sized individual grains by focused ion beam technique. *Journal of Microscopy* 235: 59-66.
- Hony S. Tielens A. G. G. M., Waters L. B. F. M., and de Koter A. 2003. The circumstellar envelope of the C-rich post-AGB star HD 56126. *Astronomy & Astrophysics* 402:211-228.
- Hoppe P., Strebel R., Eberhardt P., Amari S. and Lewis R. S. 1996. Type II supernova matter in a silicon carbide grain from the Murchison meteorite. *Science* 272:1314-1316.
- Hoppe P., Strebel R., Eberhardt P., Amari S. and Lewis R. S. 2000. Isotopic properties of silicon carbide X grains from the Murchison meteorite in the size range 0.5-1.5 mm. *Meteoritics & Planetary Science* 35:1157-1176.
- Hoppe P. and Besmehn A. 2002. Evidence for extinct vanadium-49 in presolar silicon carbide grains from supernovae. *The Astrophysical Journal* 576:L69-72.
- Hoppe P., Fujiya W., Zinner E. 2012. Sulfur molecule chemistry in supernova ejecta by silicon carbide stardust. *The Astrophysical Journal Letters* 745:L26.
- Hoppe P., Leitner J., Kodolányi J. 2015. New constraints on the abundances of silicate and oxide grains from supernovae in the acfer 094 meteorite. *The Astrophysical Journal Letters* 808:L9.
- Hoppe P., Leitner J., Kodolányi J., and Vollmer C. 2021 Isotope Systematics of Presolar

- Silicate Grains: New Insights from Magnesium and Silicon. *The Astrophysical Journal* 913, 10–26.
- Hughes J. P., Rakowski C.E., Burrows D. N. and Slane P. O. 2000 Nucleosynthesis and mixing in Cassiopeia A. *The Astrophysical Journal* 528:L109-L113.
- Huss G. R., Fahey A. J., Gallino R., and Wasserburg G. J. 1994. Oxygen isotopes in circumstellar Al₂O₃ grains from meteorites and stellar nucleosynthesis. *The Astrophysical Journal* 430:L81–L84.
- Hynes K. M. and Gyngard F. 2009. The presolar grain database (abstract #1198). 40th Lunar and Planetary Science Conference.
- Hovmöller S. 1992. Crisp—Crystallographic image-processing on a personal-computer. *Ultramicroscopy* 41:121–135.
- Jeong K. S., Winters J. M., Le Bertre T. and Sedlmayer E. 2003. Self-consistent modeling of the outflow from the O-rich Mira IRC-20197. *Astronomy & Astrophysics* 407:191-206.
- Jones A. P. and Nuth J. A. 2011. Dust destruction in the ISM: a re-evaluation of dust lifetimes. *Astronomy & Astrophysics* 530:A44.
- Keller L. P. and Messenger S. 2011. On the origins of GEMS grains. *Geochimica et Cosmochimica Acta* 75:5336-5365.
- Keller L. P. and Rahman, Z. 2011. Irradiation of FeS: Relative sputtering rates of troilite and Mg silicates (abstract #5455). *Meteoritics and Planetary Science* 74.
- Kemper F., Vriend W. J. and Tielens A. G. G. M. 2004. The Absence of Crystalline Silicates in the Diffuse Interstellar Medium. *The Astrophysical Journal* 609:826-837.
- Kifonidis K., Plewa T., Janka H. T. and Mueller E. 2003. Non-spherical core collapse supernovae. I. Neutrino-driven convection, Rayleigh-Taylor instabilities, and the formation and propagation of metal clumps. *Astronomy & Astrophysics* 408:621-649.
- Köhler M., Jones A., Ysard N. 2014. A hidden reservoir of Fe/FeS in interstellar silicates? *Astronomy & Astrophysics*, 565:L9.
- Lauretta D. S., Kremser D. T. and Fegley B., Jr. 1996. The rate of iron sulfide formation in the solar nebula. *Icarus* 122:288-315.
- Lauretta D. S., Lodders K. and Fegley B., Jr. 1997. Experimental simulations of sulfide formation in the solar nebula. *Science* 277:358-360.
- Lauretta D. S., Lodders K. and Fegley B., Jr. 1998. Kamacite sulfurization in the solar nebula. *Meteoritics & Planetary Science* 33:821-833.

- Leitner J., Vollmer C., Hoppe P. and Zipfel J. 2012a. Characterization of presolar material in the CR chondrite Northwest Africa 852. *The Astrophysical Journal* 745:38-54.
- Leitner J., Metzler K. and Hoppe P. 2014. Characterization of presolar grains in cluster chondrite clasts from unequilibrated ordinary chondrites (abstract #1099). 45th Lunar and Planetary Science Conference.
- Leitner J., Vollmer C., Floss C., Zipfel J. and Hoppe P. 2016. Ancient stardust in fine-grained chondrule rims from carbonaceous chondrites. *Earth and Planetary Science Letters* 434, 117-128.
- Leitner J., Hoppe P., Floss C., Hillion F., Henkel T. 2018. Correlated nanoscale characterization of a unique complex oxygen-rich stardust grain: Implications for circumstellar dust formation. *Geochimica et Cosmochimica Acta* 221:255-274.
- Leitner J. and Hoppe P. 2019. A new population of dust from stellar explosions among meteoritic stardust. *Nature Astronomy* 3:725-729.
- Leitner J., Metzler K., Vollmer C., Floss C., Haenecour P., Kodolányi J., Harries D., Hoppe P. 2020. The presolar grain inventory of fine-grained chondrule rims in the Mighei-type (CM) chondrites. *Meteoritics & Planetary Science* 55:1176-1206.
- Lin Y., Amari S. and Pravdivtseva O. 2002. Presolar grains from the Qingzhen (EH3) meteorite. *The Astrophysical Journal* 575:257-263.
- Lodders K. and Fegley B., Jr. 1995. The origin of circumstellar silicon carbide grains found in meteorites. *Meteoritics* 30, 661-678.
- Lodders K. 2003. Solar system abundances and condensation temperatures of the elements. *The Astrophysical Journal* 591:1220-1247.
- Lugaro M., Karakas A.I., Bruno C.G., Aliotta M., Nittler L. R., Bemmerer D., Best A., Boeltzig A., Brogгинi C., Cacioli A., Cavanna F., Ciani G.F., Corvisiero P., Davinson T., Depalo R., Leva A.D., Elekes Z., Ferraro F., Formicola A., Fulop Z., Gervino G., Guglielmetti A., Gustavino C., Gyurky G., Imbriani G., Junker M., Menegazzo R., Mossa V., Pantaleo F.R., Piatti D., Prati, P. Scott D.A., Staniero O., Strieder F., Szucs T., Takacs M.P. and Trezzi D. 2017. Origin of meteoritic stardust unveiled by revised proton-capture rate of ¹⁷O. *Nature Astronomy* 1:1-5.
- MacPherson G. J., Davis A. M. and Zinner E. K. 1995. The distribution of aluminum-26 in the early Solar System - A reappraisal. *Meteoritics* 30:365-386.
- Messenger S., Keller L. P., Stadermann F. J., Walker R. M. and Zinner E. 2003. Samples of stars beyond the solar system: Silicate grains in interplanetary dust. *Science* 300:105-108.
- Messenger S., Keller L. P. and Lauretta D. S. 2005. Supernova Olivine from Cometary Dust.

Science 309:737-741.

Meyer B. and Zinner E. 2006. Nucleosynthesis. In *Meteorites and the early solar system II*, edited by Lauretta D. S. and McSween Jr. H. Y. Tucson, Arizona: University of Arizona Press. pp. 69–108.

Molster F. J., Waters L. B. F. M. and Tielens A. G. G. M. 2002a. Crystalline silicate dust around evolved stars. II. The crystalline silicate complexes. *Astronomy & Astrophysics* 382:222-240.

Molster F. J., Waters L. B. F. M. and Tielens A. G. G. M., Koike C. and Chihara H. 2002b. Crystalline silicate dust around evolved stars. *Astronomy & Astrophysics* 382:241-255.

Molster F. and Kemper C. 2005. Crystalline Silicates. *Space Science Reviews* 119:3-28.

Mostefaoui S. and Hoppe P. 2004. Discovery of abundant in situ silicate and spinel grains from red giant stars in a primitive meteorite. *The Astrophysical Journal* 613:L149-L152.

Nagashima K., Krot A. N. and Yurimoto H. 2004. Stardust silicates from primitive meteorites. *Nature* 428:921-924.

Nguyen A. N. and Zinner E. 2004. Discovery of ancient silicate stardust in a meteorite. *Science* 303:1496-1499.

Nguyen A. N., Stadermann F. J., Zinner E., Stroud R. M., Alexander C. M. O'D. and Nittler L.R. 2007. Characterization of presolar silicate and oxide grains in primitive carbonaceous chondrites. *The Astrophysical Journal* 656:1223-1240.

Nguyen A. N., Nittler L. R., Stadermann F. J., Stroud R. M. and Alexander C. M. O'D. 2010. Coordinated analyses of presolar grains in the Allan Hills 77307 and Queen Elizabeth range 991777 meteorites. *The Astrophysical Journal* 719:166-189.

Nguyen A. N., Keller L. P., Rahman Z. and Messenger S. 2013. Crystal structure and chemical composition of a presolar silicate from the Queen Elizabeth Range 99177 meteorite (abstract #2853). 44th Lunar and Planetary Science Conference.

Nguyen A. N. and Messenger S. 2014a. Resolving the stellar sources of isotopically rare presolar silicate grains through Mg and Fe isotopic analyses. *The Astrophysical Journal* 784:149.

Nguyen A. N., Nakamura-Messenger K., Messenger S., Keller L. P. and Klöck W. 2014b. Identification of a compound spinel and silicate presolar grain in a chondritic interplanetary dust particle (abstract #2351). 45th Lunar and Planetary Science Conference.

- Nguyen A. N., Keller L. and Messenger S. 2016. Mineralogy of Presolar Silicate and Oxide Grains of Diverse Stellar Origins. *The Astrophysical Journal* 818:51.
- Nguyen A. N., Keller L., Messenger S. and Rahman Z. 2017. Mineralogical characterization of Fe-bearing AGB and supernova grains from the queen alexandra range 99177 meteorite (abstract#2371). 48th Lunar and Planetary Science Conference.
- Nittler L. R., Alexander C. M. O'D., Gao X., Walker R. M. and Zinner E. 1994. Interstellar oxide grains from the Tieschitz ordinary chondrite. *Nature* 370:443-446.
- Nittler L. R., Hoppe P., Alexander C. M. O'D., Amari S., Eberhardt P., Gao, X., Lewis, R. S., Strebel, R., Walker, R. M. and Zinner, E. 1995. Silicon nitride from supernovae. *The Astrophysical Journal* 453:L25-28.
- Nittler L. R., Amari S., Zinner E., Woosley S. E. and Lewis R. S. 1996. Extinct ^{44}Ti in presolar graphite and SiC: Proof of a supernova origin. *The Astrophysical Journal* 462:L31-34.
- Nittler L. R., Alexander C. M. O'D., Gao X., Walker R. M. and Zinner E. 1997. Stellar sapphires: The properties and origins of presolar Al_2O_3 in meteorites. *The Astrophysical Journal* 483:475-495.
- Nittler L. R., Alexander C. M. O'D., Wang J. and Gao X. 1998. Meteoritic oxide grain from supernova found. *Nature* 393:222.
- Nittler L. R. and Dauphas N. D. 2006. Meteorites and the Chemical Evolution of the Milky Way. In: *Meteorites and the Early Solar System II*, edited by Lauretta, D.S., McSween Jr., H.Y. Tucson, Arizona: University of Arizona Press, pp. 127-146.
- Nittler L. R., Alexander C. M. O'D., Gallino R., Hoppe P., Nguyen A. N., Stadermann F. and Zinner, E. K. 2008. Aluminum-, Calcium- and Titanium rich oxide stardust in ordinary chondrite meteorites. *The Astrophysical Journal* 682:1450-1478.
- Nittler L. R. and Ciesla F. 2016. Astrophysics with extraterrestrial materials. Annual Reviews in *Astronomy & Astrophysics* 54:53-93.
- Nittler L. R., Alexander C. M. O'D., Davidson J., Riebe M., Stroud R. and Wang J. 2018. High abundances of presolar grains and ^{15}N -rich organic matter in the CO3.0 chondrite Dominion Range 08006. *Geochimica et Cosmochimica Acta* 226:107-131.
- Nittler L. R., Stroud R. M., Alexander C. M. O'D. and Howell K. 2020. Presolar grains in primitive ungrouped carbonaceous chondrite Northwest Africa 5958. *Meteoritics & Planetary Science* 55:1160-1175.
- Nittler L. R., Alexander C. M. O'D. Patzer A., Verdier-Paoletti M. 2021. Presolar stardust in the highly pristine CM chondrites Asuka 12169 and Asuka 12236. *Meteoritics*

& *Planetary Science* 56:260-276.

- Nollett K. M., Busso M. and Wasserburg G. J. 2003. Cool bottom processes on the thermally-pulsing AGB and the isotopic composition of circumstellar dust grains. *The Astrophysical Journal* 582:1036-1058.
- Nozawa T., Kozasa T., Umeda H., Maeda K. and Nomoto K. 2003. Dust in the early universe: dust formation in the ejecta of population III supernovae. *The Astrophysical Journal* 589:785-803.
- Ong W. J. and Floss C. 2015. Iron isotopic measurements in presolar silicate and oxide grains from the Acfer 094 ungrouped carbonaceous chondrite. *Meteoritics & Planetary Science* 50: 1392-1407.
- Rauscher T., Heger A., Hoffman R. D. and Woosley S. E. 2002. Nucleosynthesis in massive stars with improved nuclear and stellar physics. *The Astrophysical Journal* 576:323-348.
- Rho J., Kozasa T., Reach W. T., Smith J. D., Rudnick L., DeLaney T., Ennis J. A., Gomez H. and Tappe A. 2008. Freshly Formed Dust in the Cassiopeia A Supernova Remnant as Revealed by the Spitzer Space Telescope. *The Astrophysical Journal* 673:271-282.
- Rho J., Reach W. T., Tappe A., Hwang U., Slavin J.D., Kozasa T. and Dunne L. 2009. Spitzer observations of the young core-collapse supernova remnant 1E0102-72.3: infrared ejecta and dust formation. *The Astrophysical Journal* 700:579-596.
- Scott E. R. D. and Krot A. N. 2014. Chondrites and their components. In *Treatise on Geochemistry* (2nd ed.), edited by Turekian H. D. H. K. Oxford: Elsevier. pp. 65–137.
- Seifert L. B., Haenecour P., Zega T. J. and Floss C. 2018. TEM analysis of a presolar silicate grain in the Dominion Range 08006, CO chondrite (abstract #2980). 49th Lunar and Planetary Science Conference.
- Seifert L. B., Haenecour P. and Zega T. J. 2019. Elemental composition and microstructure of a supernova polycrystalline olivine aggregate in the CO chondrite Dominion Range 08006 (abstract #2585). 50th Lunar and Planetary Science Conference.
- Seifert L. B., Haenecour P., Ramprasad T. and Zega T. J. 2020. Structure and chemistry of a supernova orthopyroxene grain in the CO chondrite Dominion Range 08006 (abstract #2471). 51st Lunar and Planetary Science Conference.
- Speck A. K., Barlow M. J., Sylvester R. J. and Hofmeister A. M. 2000. Dust features in the 10- μ m infrared spectra of oxygen-rich evolved stars. *Astronomy & Astrophysics Supplement Series* 146:437-464.
- Stroud R. M., Nittler L. R. and Alexander C. M. O'D. 2004. Polymorphism in presolar Al₂O₃ grains from asymptotic giant branch stars. *Science* 305:1455-1457.

- Stroud R. M., Floss C. and Stadermann F. J. 2009. Structure, elemental composition, and isotopic composition of presolar silicates in MET 00426 (abstract #1063). 40th Lunar and Planetary Science Conference.
- Stroud R. M., Nittler L. R. and Alexander C. M. O'D. 2013. Analytical electron microscopy of a CAI-like presolar grain and associated fine-grained matrix material in the Dominion Range 08006 CO3 meteorite (abstract #2315). 44th Lunar and Planetary Science Conference.
- Stroud R. M., De Gregorio B. T., Nittler L. R. and Alexander C. M. O'D. 2014. Comparative transmission electron microscopy studies of presolar silicate and oxide grains from the Dominion Range 08006 and Northwest Africa 5958 meteorites (abstract #2806). 45th Lunar and Planetary Science Conference.
- Tachibana S. and Huss G. R. 2003. The initial abundance of ^{60}Fe in the solar system. *The Astrophysical Journal Letters* 588:L41-L44.
- Takigawa A., Stroud R.M., Nittler L.R., Vicenzi E.P., Herzing A., Alexander C. M. O'D. and Huss G.R. 2014. Crystal structure, morphology, and isotopic compositions of presolar Al_2O_3 grains in unequilibrated ordinary chondrites (abstract #1465). 45th Lunar and Planetary Science.
- Tielens A. G. G. M., Waters L. B. F. M., Molster F. J. and Justtanont K. 1998. Circumstellar Silicate Mineralogy. *Astrophysics and Space Science* 255:415-426.
- Timmes F. X. and Clayton D. D. 1996. Galactic evolution of silicon isotopes: Application to presolar SiC grains from meteorites. *The Astrophysical Journal* 472:723-741.
- Tonotani A., Kobayashi S., Nagashima K., Sakamoto N., Russell S. S., Itoh S. and Yurimoto H. 2006. Presolar grains from primitive ordinary chondrites (abstract #1539). 37th Lunar and Planetary Science Conference.
- Todini P. and Ferrara A. 2001. Dust formation in primordial Type II supernovae. *Monthly Notices of the Royal Astronomical Society* 325:726-736.
- Varshneya A K. 1993. Fundamentals of Inorganic Glasses. San Diego: Elsevier Science & Technology.
- Verdier-Paoletti M. J., Nittler L. R. and Wang J. 2019. High resolution measurements of Mg, Si, Fe and Ni isotopes of O-rich presolar grains (abstract #6433). *Meteoritics & Planetary Science* 82.
- Vollmer C., Hoppe P., Brenker F. E. and Holzappel C. 2007. Stellar MgSiO_3 perovskite: A shock-transformed stardust silicate found in a meteorite. *The Astrophysical Journal* 666:L49-L52.

- Vollmer C., Hopper P., and Brenker F. E. 2008. Si isotopic compositions of presolar silicate grains from red giant stars and supernovae. *The Astrophysical Journal* 684:611-617.
- Vollmer C., Brenker F. E., Hoppe P. and Stroud, R. M. 2009. Direct laboratory analysis of silicate stardust from red giant stars. *The Astrophysical Journal* 700:774-782.
- Vollmer C., Hoppe P. and Brenker F. E. 2013. Transmission electron microscopy of Al-rich silicate stardust from asymptotic giant branch stars. *The Astrophysical Journal* 769:61-69.
- Wasserburg G. J., Boothroyd A. I. and Sackmann I. J. 1995. Deep circulation in red giant stars: A solution to the carbon and oxygen isotope puzzles? *The Astrophysical Journal Letters* 447:L37-40.
- Yada T., Floss C., Stadermann F., Zinner E., Nakamura T., Noguchi T. and Lea S. 2008. Stardust in antarctic micrometeorites. *Meteoritics & Planetary Science*. 43: 1287-1298.
- Zega T. J., Nittler L. R., Busemann H., Hoppe P. and Stroud R. M. 2007. Coordinated isotopic and mineralogical analyses of planetary materials enabled by in situ lift-out with a focused-ion-beam scanning-electron microscope. *Meteoritics & Planetary Science* 42:1373-1386.
- Zega T. J., Alexander C. M. O'D., Nittler L. R. and Stroud R. M. 2011. A transmission electron microscopy study of presolar hibonite. *The Astrophysical Journal* 730:83-93.
- Zega T. J., Nittler L. R., Gyngard F., Alexander C. M. O'D., Stroud R. M. and Zinner E. 2014. A transmission electron microscopy study of presolar spinel. *Geochimica et Cosmochimica Acta* 124:152-169.
- Zega T. J., Haenecour P., Floss C. and Stroud R. M. 2015. Circumstellar magnetite from the LAP 031117 CO3.0 chondrite. *The Astrophysical Journal* 808:1-8.
- Zega T. J., Haenecour P. and Floss C. 2020. An in situ investigation on the origins and processing of circumstellar oxide and silicate grains in carbonaceous chondrites. *Meteoritics & Planetary Science* 55:1207-1227.
- Zhao X., Stadermann F. J., Floss C., Bose M. and Lin Y. 2010. Characterization of presolar grains from the carbonaceous chondrite Ningqiang (abstract #1431). 41st Lunar and Planetary Science Conference.
- Zhao X., Floss C., Stadermann F. J., Bose M. and Lin Y. 2011. Continued investigation of presolar silicate grains in the carbonaceous chondrite Ningqiang (abstract #1982). 42nd Lunar and Planetary Science Conference.
- Zhao X., Floss C., Lin Y. and Bose M. 2013. Stardust investigation into the CR chondrite Grove Mountain 021710. *The Astrophysical Journal* 769:49.

Zinner E., Amari S., Guinness R., Nguyen A., Stadermann F. J., Walker R. M. and Lewis R. 2003. Presolar spinel grains from the Murray and Murchison carbonaceous chondrites. *Geochimica et Cosmochimica Acta* 67:5083-5095.

Zinner E., Nittler L. R., Hoppe P., Gallino R., Straniero O. and Alexander C. M. O'D. 2005. Oxygen, magnesium and chromium isotopic ratios of presolar spinel grains. *Geochimica et Cosmochimica Acta* 69:4149-4165.

Zinner E. K. 2014, Presolar Grains. In *Treatise on geochemistry volume 1: Meteorites and cosmochemical processes*, edited by Davis A. M. Amsterdam: Elsevier Ltd. pp. 181-213.

Tables and Figures

Table 1. Grain compositions determined using EDS expressed in wt% and cation count.

Grain	DOM-49	DOM-49 (Fe, Ni, S region)	DOM-59 (Shell)	DOM-59 (Core)	DOM-22 (R)	DOM-22 (Fe, Ni, S region)	DOM-35 (L)	DOM-35 (R)	DOM-39	DOM-39 (Fe, Ni, S region)	DOM-50
Phase	Olivine	Fe-sulfide	Olivine	Olivine	Silicate	Pentlandite	Olivine	Olivine	Pyroxene	Fe-sulfide	Silicate
$^{17}\text{O}/^{16}\text{O} (\times 10^{-4})$	5.3 ± 0.2	5.3 ± 0.2	11.6 ± 0.5	11.6 ± 0.5	3.8 ± 0.2	3.8 ± 0.2	4.0 ± 0.2	4.0 ± 0.2	6.2 ± 0.3	6.2 ± 0.4	3.6 ± 0.2
$^{18}\text{O}/^{16}\text{O} (\times 10^{-3})$	2.05 ± 0.04	2.05 ± 0.04	0.69 ± 0.03	0.69 ± 0.03	2.47 ± 0.05	2.47 ± 0.05	3.34 ± 0.07	3.34 ± 0.07	2.64 ± 0.07	2.64 ± 0.08	2.56 ± 0.05
Wt%											
O	36.84	28.98	44.59	44.15	41.17	n.d.	43.95	43.05	39.78	n.d.	30.19
Si	18.16	17.41	19.72	20.20	20.01	n.d.	19.87	18.83	21.71	n.d.	7.86
Mg	6.12	5.65	32.03	27.16	18.16	n.d.	27.66	27.02	7.75	n.d.	7.84
Fe	33.05	35.78	3.67	1.16	18.20	48.04	6.70	10.04	24.10	74.56	52.17
Ca	1.15	1.68	n.d.	7.34	n.d.	n.d.	0.87	n.d.	n.d.	n.d.	0.62
Al	1.50	1.46	n.d.	n.d.	0.87	n.d.	0.96	1.06	1.99	n.d.	n.d.
S	n.d.	3.03	n.d.	n.d.	n.d.	27.63	n.d.	n.d.	n.d.	12.67	n.d.
Ni	3.18	6.02	n.d.	n.d.	1.60	24.33	n.d.	n.d.	4.67	12.77	n.d.
Ti	n.d.	n.d.	n.d.	n.d.	n.d.	n.d.	n.d.	n.d.	n.d.	n.d.	1.32
Cation											
O	4	n.d.	4	4	12	n.d.	4	4	3	n.d.	12
Si	1.12	n.d.	1.01	1.04	3.32	n.d.	1.03	1.0	0.93	n.d.	1.78
Mg	0.44	n.d.	1.89	1.62	3.48	n.d.	1.66	1.65	0.38	n.d.	2.05
Fe	1.03	n.d.	0.09	0.03	1.52	6.68	0.17	0.27	0.52	1.37	5.94
Ca	0.05	n.d.	n.d.	0.27	n.d.	n.d.	0.03	n.d.	n.d.	n.d.	0.10
Al	0.10	n.d.	n.d.	n.d.	0.15	n.d.	0.05	0.06	0.09	n.d.	n.d.
S	n.d.	n.d.	n.d.	n.d.	n.d.	6.69	n.d.	n.d.	n.d.	0.405	n.d.
Ni	0.09	n.d.	n.d.	n.d.	0.13	3.22	n.d.	n.d.	0.10	0.22	n.d.
Ti	n.d.	n.d.	n.d.	n.d.	n.d.	n.d.	n.d.	n.d.	n.d.	n.d.	0.18

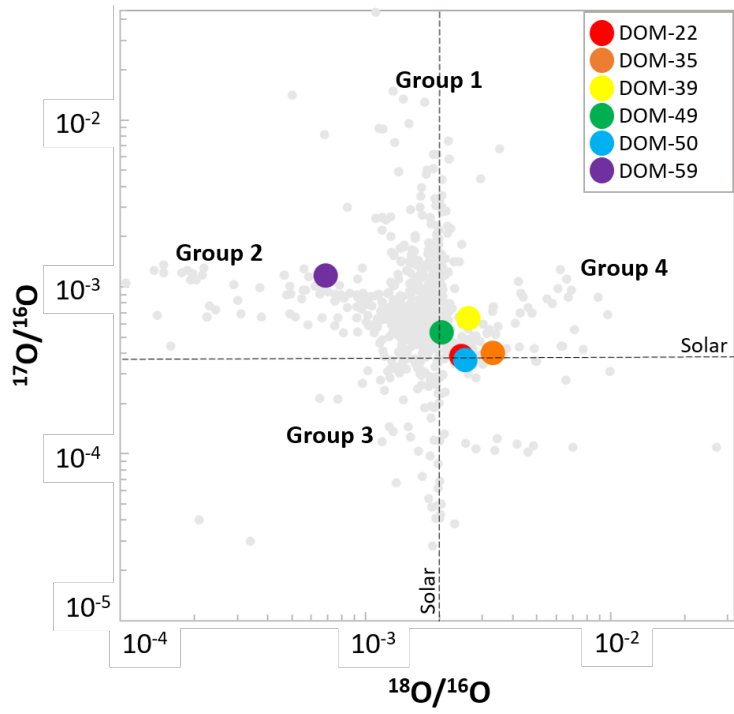
O-isotopic compositions from Haeneccour et al. (2018). All analyses normalized to 100%.
L and R refer to left and right sides of grain.
n.d. = not detected.

Table 2. d-spacings determined by SAED.

Grain	Ring Number	d (Å)	<i>hkl</i>	Reference d-spacing (Å)
DOM-22	1	2.53	611	2.52 (px)
DOM-22	2	2.13	630	2.12 (px)
DOM-22	3	1.51	320	1.51 (ol)
DOM-22	4	1.22	342, 353	1.22 (ol, px)
DOM-35	1	3.72	101	3.72 (ol)
DOM-35	2	2.78	130	2.77 (ol)
DOM-35	3	2.26	122	2.26 (ol)
DOM-35	4	2.09	132	2.03 (ol)
DOM-35	5	1.73	240	1.73 (ol)
DOM-35	6	1.47	062	1.47 (ol)
DOM-50	1	2.96	321	2.96 (px)
DOM-50	2	2.33	041	2.34 (ol)
DOM-50	3	1.73	240	1.73 (ol)
DOM-50	4	1.29	063, 661	1.29 (ol, px)
DOM-50	5	1.13	122, 711	1.13 (ol, px)
DOM-50	6	0.95	315, 535	0.95 (ol, px)

See Figs. 5, 6, and 8 for locations of rings in SAED patterns.

Figure 1.



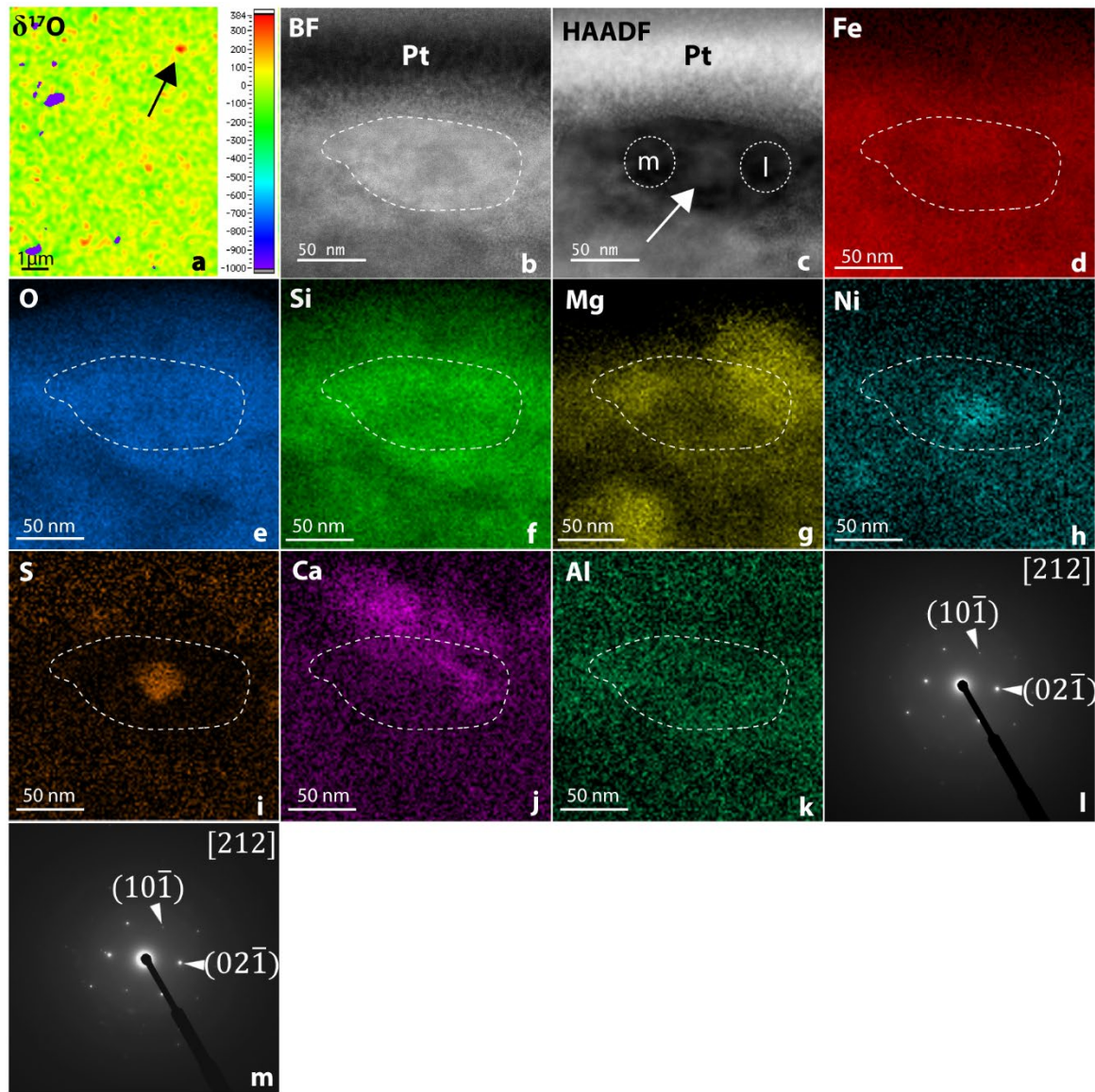


Figure 2.

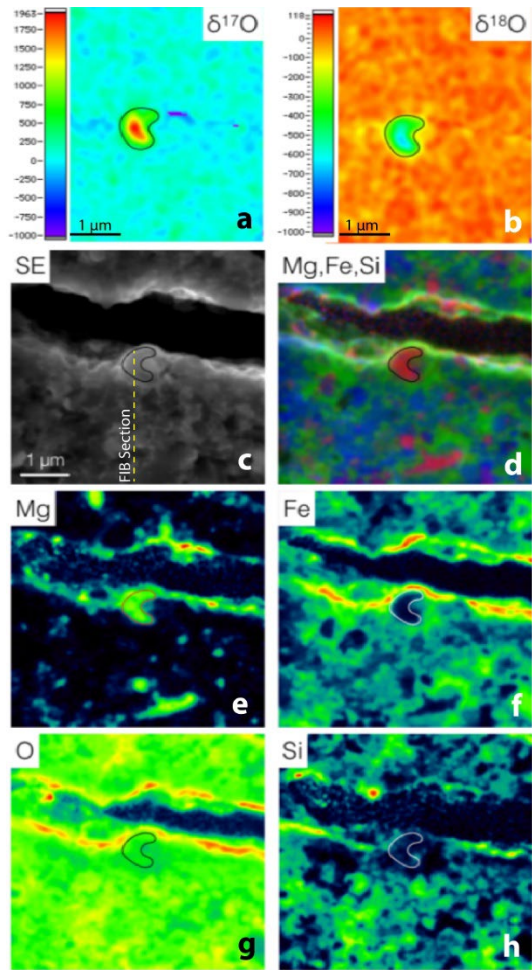


Figure 3.

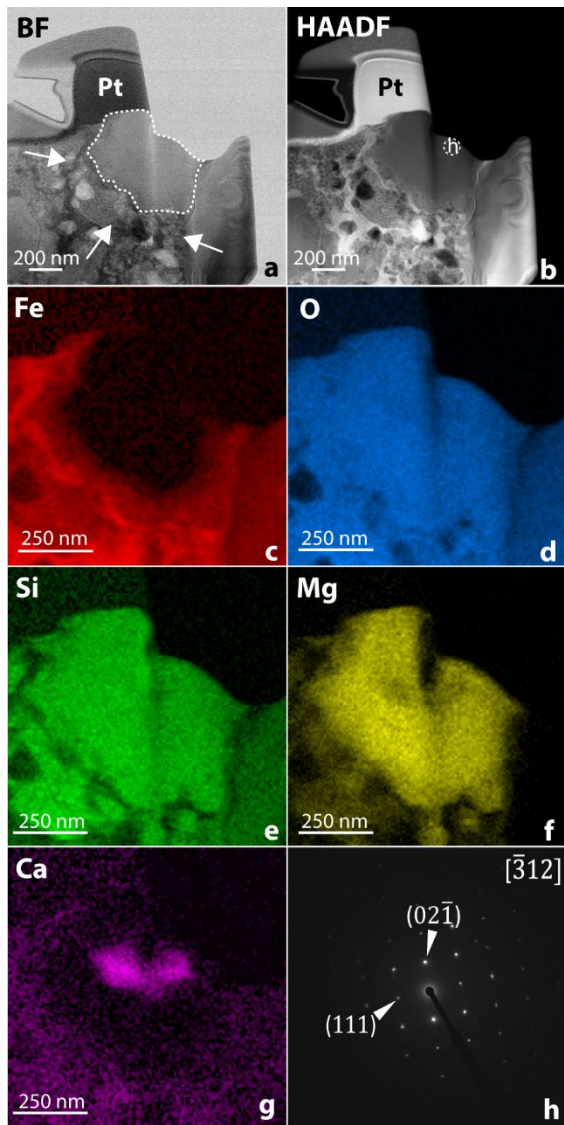


Figure 4.

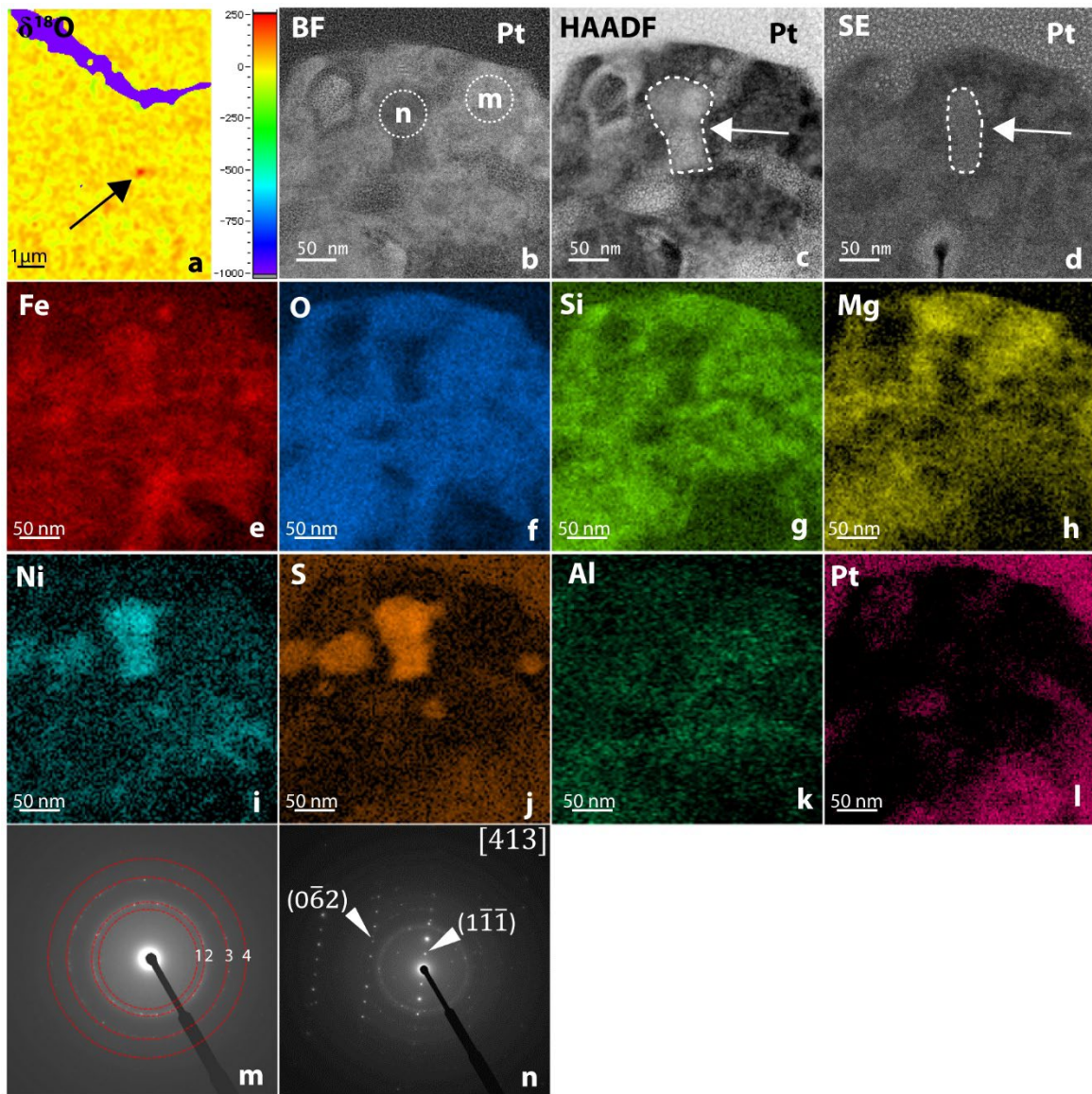


Figure 5.

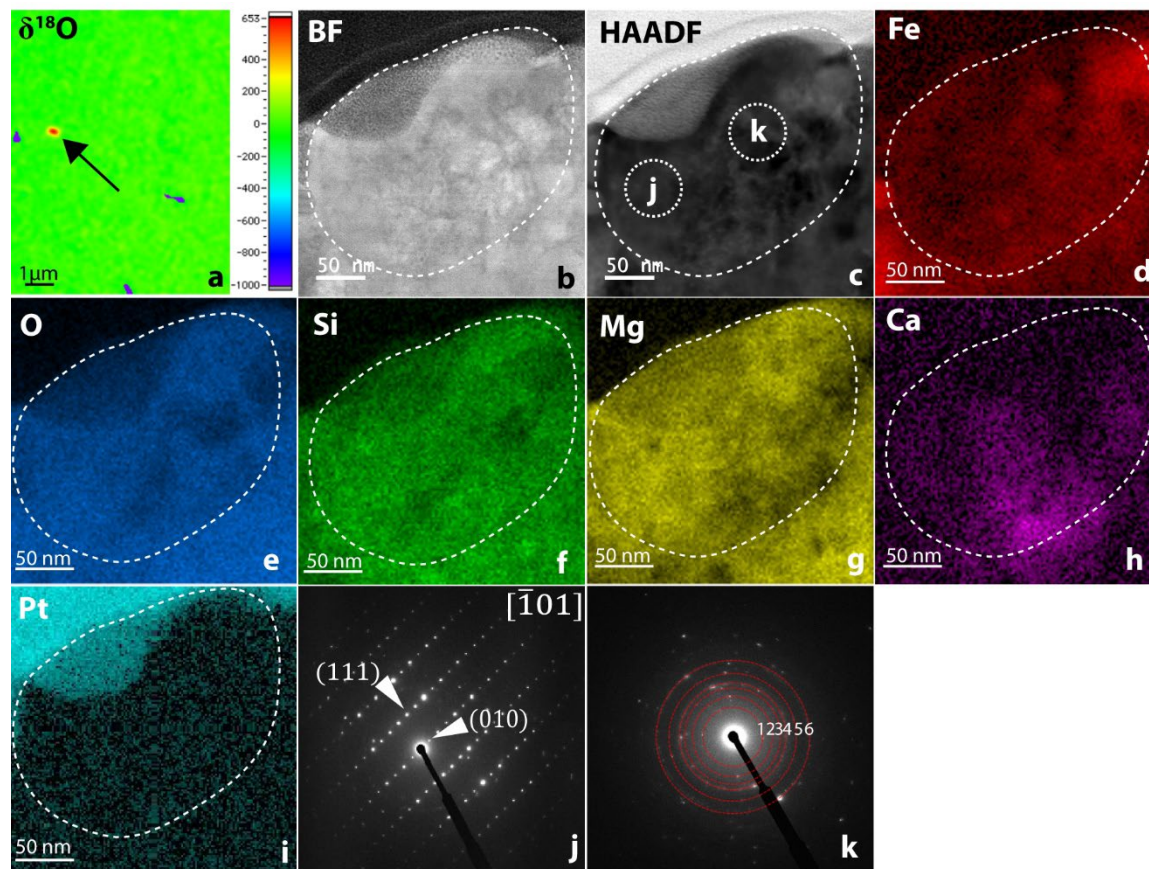


Figure 6.

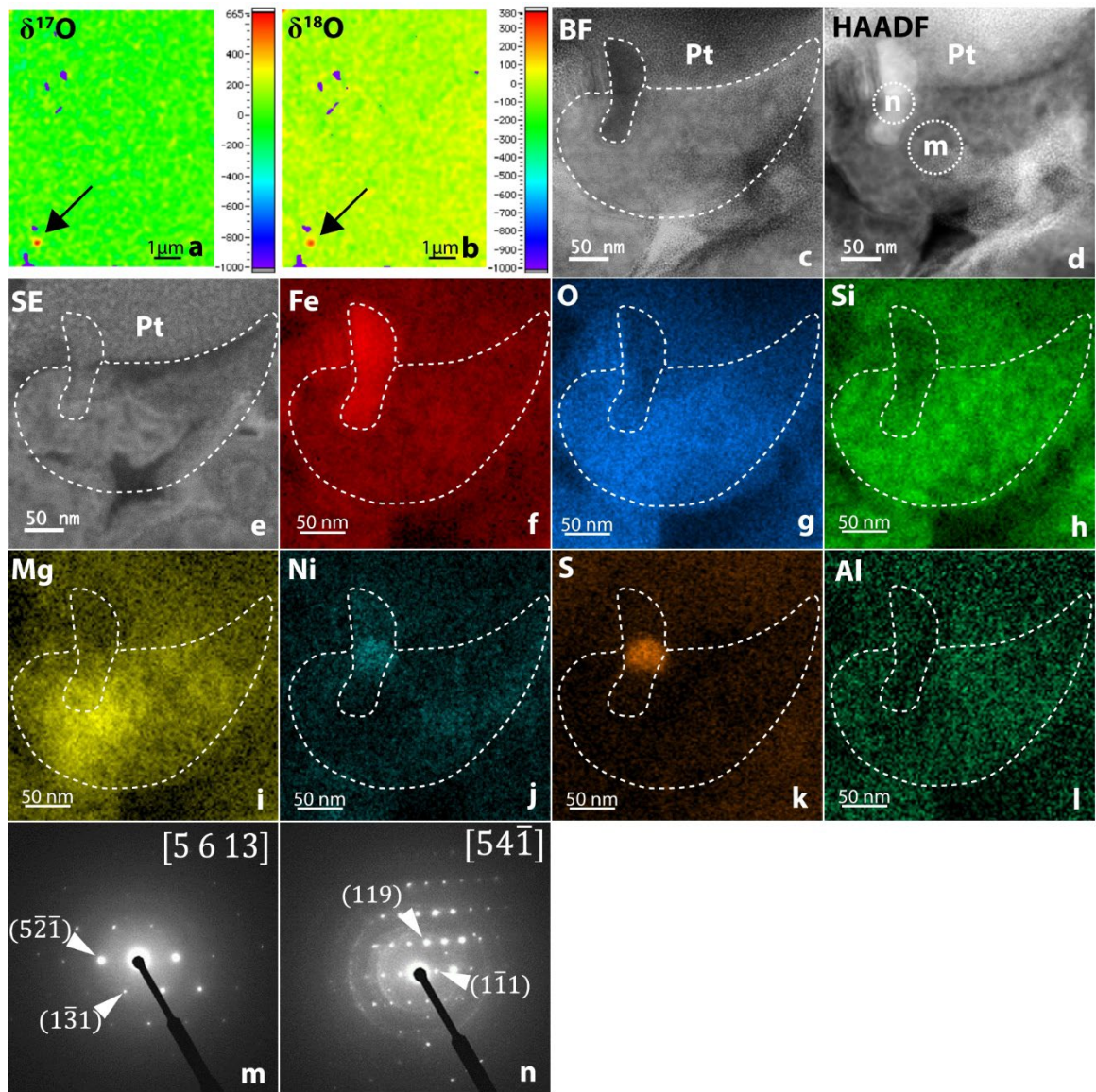


Figure 7.

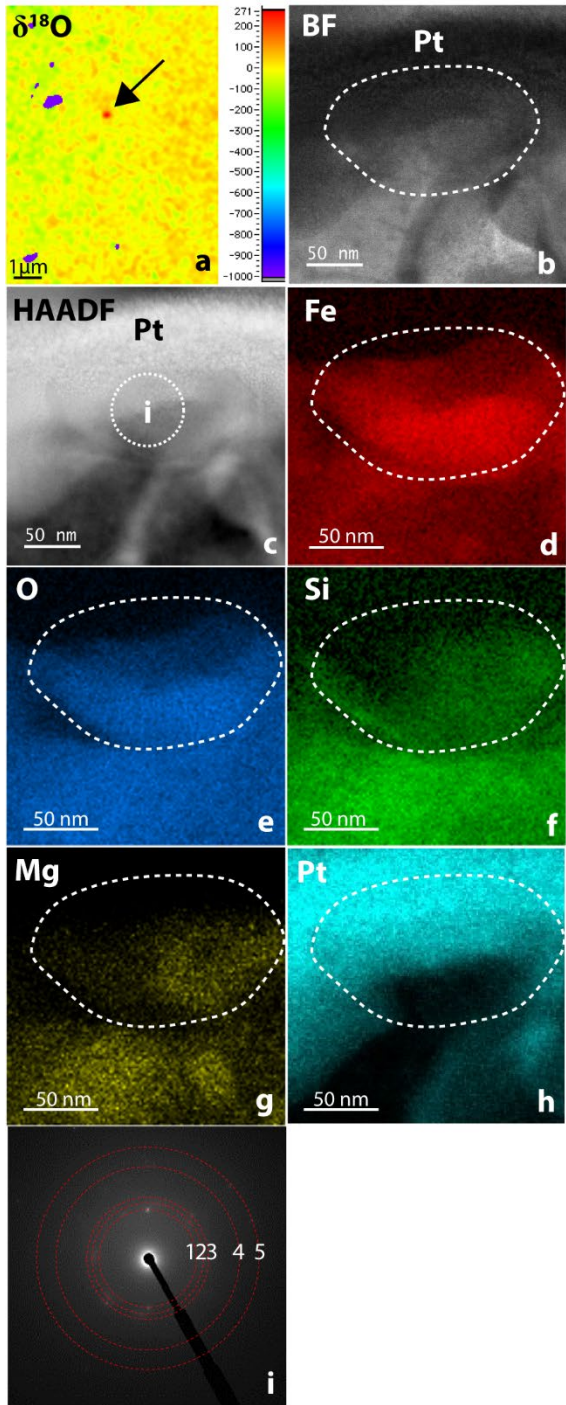


Figure 8.

Figure. 1. Three O-isotope plot with presolar grains in this study represent by colored circles. Other presolar silicate and oxide grains are plotted for reference in gray circles (literature data from Nittler et al. 1994, 1997, 1998, 2008, 2018; Huss et al. 1994; Choi et al. 1998, 1999; Zinner et al. 2003, 2005; Messenger et al. 2003, 2005; Mostefaoui & Hoppe 2004; Nagashima et al. 2004; Nguyen & Zinner 2004; Tonotani et al. 2006; Ebata et al. 2006; Floss et al. 2006, 2010, 2013; Nguyen et al. 2007, 2010; Busemann et al. 2009; Floss & Stadermann 2009a, 2009b, 2012; Vollmer et al. 2009; Gyngard et al. 2010a, 2010b; Bose et al. 2010, 2012, 2014; Zhao et al. 2010, 2011, 2013; Keller & Messenger 2011; Leitner et al. 2012a, 2014, 2016, 2020; Davidson et al. 2014, 2015; Floss & Haenecour 2016; Haenecour et al. 2018 and the Presolar Grain Database, Hynes & Gyngard 2009). Solar composition represented by dashed lines.

Figure. 2. NanoSIMS and TEM data on DOM-49. (a) NanoSIMS $\delta^{17}\text{O}$ (delta notation denotes the deviation of an isotopic ratio of an element R from a standard [$\delta R = ((R_{\text{measured}}/R_{\text{standard}}) - 1) \times 1000$], where R is the ratio of the heavy to light isotope) map of DOM-49, with legend at right of image in units of per mil (‰). (b) BF STEM image with dashed line indicating DOM-49 below Pt fiducial marker (we note that dashed line is not meant to be absolute, but rather guide the reader to the ROI). (c) HAADF STEM image with arrow indicating brighter contrast center. (d-k) False color EDS maps for Fe, O, Si, Mg, Ni, S, Ca, Al, respectively. (l-m) SAED pattern from region denoted by (l) and (m) in HAADF image.

Figure. 3. Auger nanoprobe data on DOM-59. (a-b) NanoSIMS $\delta^{17}\text{O}$ and $\delta^{18}\text{O}$ maps of DOM-59, with legend at left of image in units of per mil (‰). (c) SE image of DOM-59 with anomalous region outlined and FIB transect highlighted by dashed line. (d-h) false color Auger elemental maps as indicated by upper left corner of image.

Figure. 4. TEM data on DOM-59. (a) BF STEM image with dashed line indicating location of DOM-59 (we note that dashed line is not meant to be absolute, but guide the reader to the ROI) and arrows indicating textural change outside of DOM-59. (b) HAADF STEM image of DOM-59, with Pt marker indicated. (c-g) False color EDS maps of Fe, O, Si, Mg, Ca, respectively. (h) SAED pattern acquired from region (h) as shown in the HAADF image.

Figure. 5. NanoSIMS and TEM data on DOM-22. (a) NanoSIMS $\delta^{18}\text{O}$ map of DOM-22, with legend at right of image in units of per mil (‰). (b) BF STEM image with DOM-22 located below Pt fiducial marker. (c) HAADF STEM image with bright contrast feature indicated by arrow. (d) SE STEM image with Pt fiducial marker labeled. (e-l) False color EDS maps of DOM-22 for Fe, O, Si, Mg, Ni, S, Al, Pt, respectively. (m) SAED pattern acquired from region (m) shown in BF image with rings labeled 1-4. (n) SAED pattern acquired from region (n) shown in BF image.

Figure. 6. NanoSIMS and TEM data on DOM-35. (a) NanoSIMS $\delta^{18}\text{O}$ map of DOM-35, with legend at right of image in units of per mil (‰). (b-c) BF and HAADF images with DOM-35

highlighted by dashed oval (we note that dashed oval is not meant to be absolute, but rather guide the reader to the ROI). (d-i) False color EDS maps of DOM-35 for Fe, O, Si, Mg, Ca, Pt, respectively. The high contrast feature in the BF and HAADF images (b-c) spatially correlates with Pt (i) and is the result of Pt redeposition during the final thinning of the FIB section. (j) SAED pattern acquired from region labeled (j) in HAADF image. (k) SAED pattern acquired from region labeled (k) in HAADF image with rings labeled 1-6.

Figure. 7. NanoSIMS and TEM data on DOM-39. (a-b) NanoSIMS $\delta^{17}\text{O}$ and $\delta^{18}\text{O}$ maps of DOM-39, with legend at right of image in units of per mil (‰). (c) BF STEM image with DOM-39 indicated by dashed line below Pt fiducial marker (we note that dashed line is not meant to be absolute, but rather guide the reader to the ROI). (d-e) HAADF and SE STEM images of DOM-39 below Pt fiducial marker. (f-l) False color EDS maps of DOM-39 for Fe, O, Si, Mg, Ni, S, Al, respectively. (m) SAED pattern acquired from region labeled (m) in HAADF image. (n) SAED pattern acquired from region labeled (n) in HAADF image.

Figure. 8. NanoSIMS and TEM data on DOM-50. (a) NanoSIMS $\delta^{18}\text{O}$ maps of DOM-50, with legend at right of image in units of per mil (‰). (b) BF STEM image with DOM-50 indicated by dashed oval below Pt fiducial marker (we note that dashed oval is not meant to be absolute, but rather guide the reader to the ROI). (c) HAADF STEM image of DOM-50. (d-h) False color EDS maps of DOM-50 for Fe, O, Si, Mg, Pt, respectively. (i) SAED pattern acquired from region labeled (i) in HAADF image with rings labeled 1-5.

Supporting Data

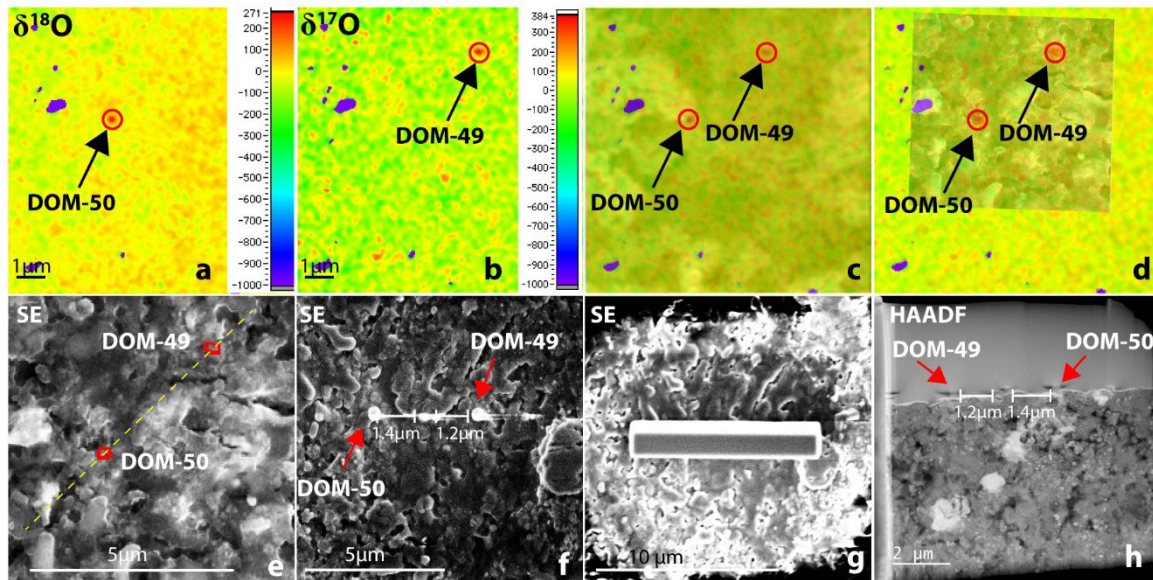


Figure 9.

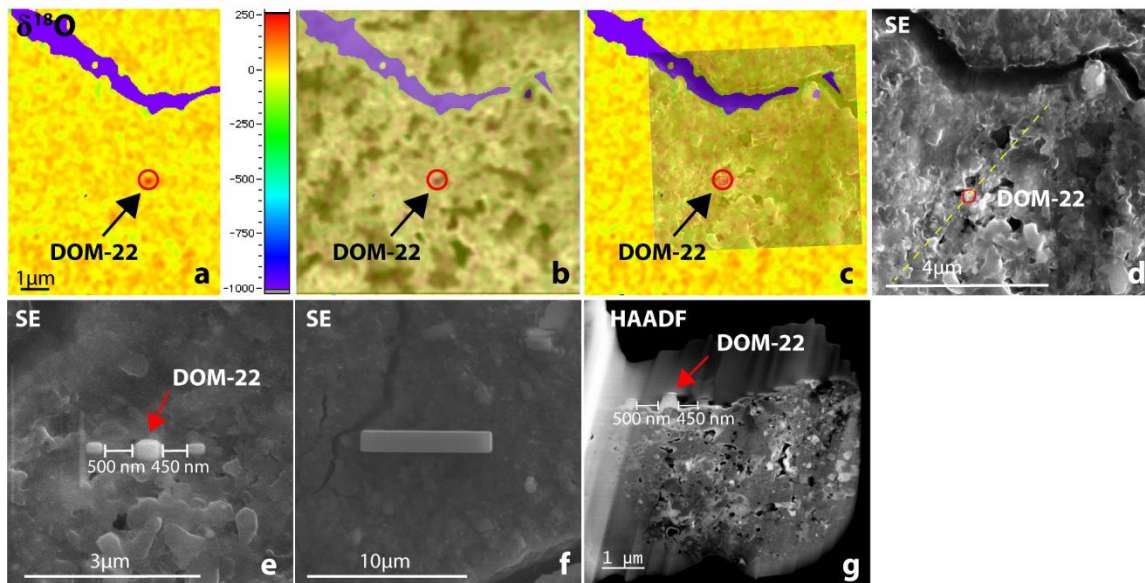


Figure 10.

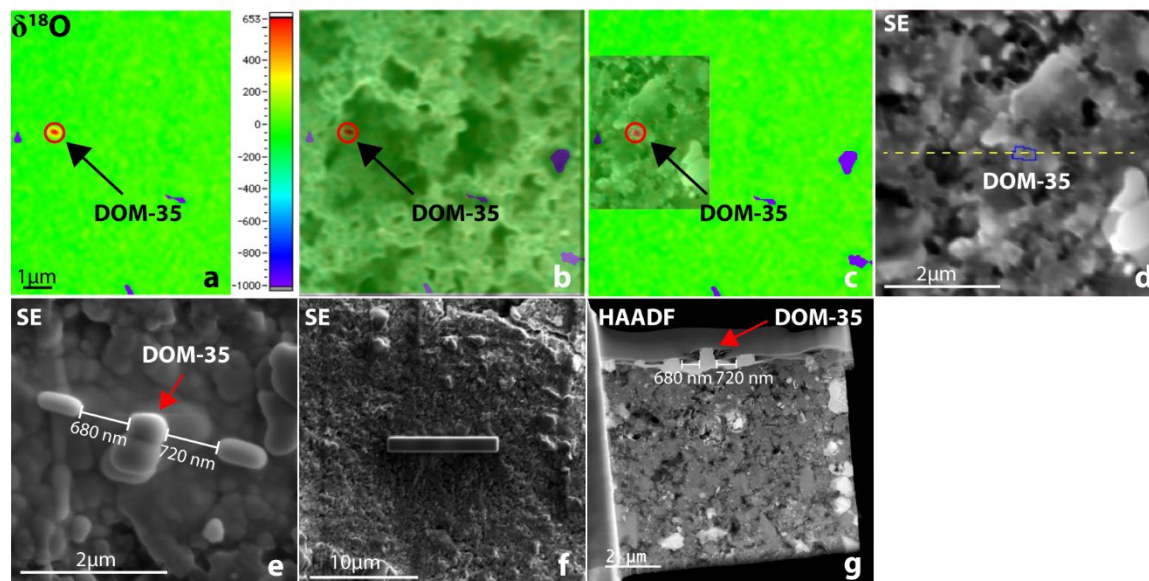


Figure 11.

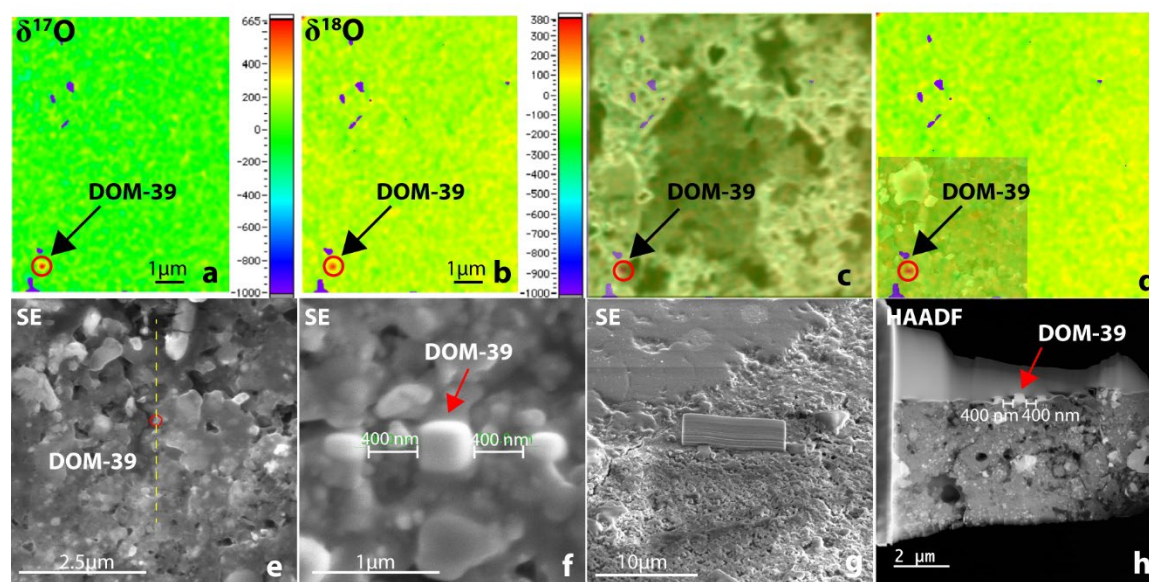


Figure 12.

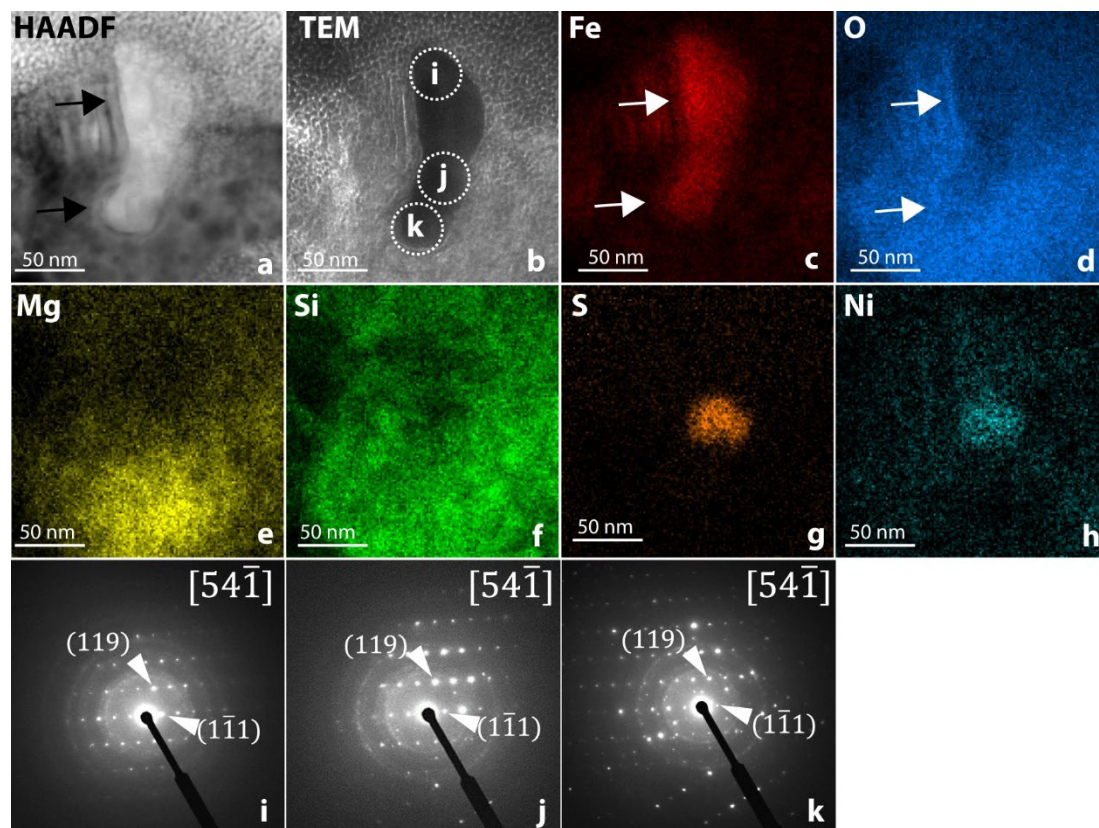


Figure 13.

Supporting Data Figure Captions

Figure 9. NanoSIMS and FIB-SEM grain alignment and Pt fiducial marker placement for DOM-49 and DOM-50. To confirm the grain alignment from the ImageAlign software, the SE FIB-SEM image was made semi-transparent, scaled appropriately, and overlaid onto the SE NanoSIMS image. The SE NanoSIMS and FIB-SEM images were then overlaid onto the O-isotope maps to confirm that the grain alignments match the isotope anomaly. The same procedure was used for all subsequent grains. a-b) NanoSIMS $\delta^{18}\text{O}$ and $\delta^{17}\text{O}$ maps with DOM-49 and DOM-50 indicated by arrows. Legend at right of image in units of per mil (‰). c) Semi-transparent $\delta^{18}\text{O}$ and $\delta^{17}\text{O}$ maps showing the location of anomalous grains with overlay of the corresponding SE NanoSIMS image. d) NanoSIMS $\delta^{18}\text{O}$ and $\delta^{17}\text{O}$ maps with semi-transparent overlay of the SE FIB-SEM image confirming the correct alignment of DOM-49 and DOM-50. e) SE image with aligned anomalous regions DOM-49 and DOM-50 labeled and outlined in red. Dotted yellow line indicates FIB transect. f) SE image of Pt fiducial markers with DOM-49 and DOM-50 grain fiducials indicated by red arrows. Distances between fiducial markers labeled. g) SE image of protective C capping layer before FIB trenching and liftout. h) HAADF STEM image of FIB section containing DOM-49 and DOM-50. Distances between markers labeled and grain fiducials indicated by red arrows.

Figure 10. NanoSIMS and FIB-SEM grain alignment and Pt fiducial marker placement for DOM-22. a) NanoSIMS $\delta^{18}\text{O}$ map of DOM-22, with legend at right of image in units of per mil (‰). b) $\delta^{18}\text{O}$ map showing the location of the anomalous grain with semi-transparent overlay of the corresponding SE NanoSIMS image. c) NanoSIMS $\delta^{18}\text{O}$ map with semi-transparent overlay of the SE FIB-SEM image confirming the correct alignment of DOM-22. d) SE FIB-SEM image with anomalous region outlined in red, dotted yellow line indicates FIB transect. e) SE image of Pt fiducial markers with the DOM-22 grain fiducial indicated by red arrow. Distances between fiducial markers labeled. f) SE image of protective C capping layer before FIB trenching and liftout. g) HAADF STEM image of the FIB section containing DOM-22 with distances between markers labeled and grain fiducial indicated by red arrow.

Figure 11. NanoSIMS and FIB-SEM grain alignment and Pt fiducial marker placement for DOM-35. a) NanoSIMS $\delta^{18}\text{O}$ map of DOM-35, with legend at right of image in units of per mil (‰). b) $\delta^{18}\text{O}$ map showing the location of the anomalous grain with semi-transparent overlay of the corresponding SE NanoSIMS image. c) NanoSIMS $\delta^{18}\text{O}$ map with semi-transparent overlay of the SE FIB-SEM image confirming the correct alignment of DOM-35. d) SE FIB-SEM image with anomalous region outlined in blue, dotted yellow line indicates FIB transect. e) SE image of Pt fiducial markers with the DOM-35 grain fiducial indicated by red arrow. Distances between fiducial markers labeled. f) SE image of protective C capping layer before FIB trenching and liftout. g) HAADF STEM image of FIB section containing DOM-35 with distances between markers labeled and grain fiducial indicated by red arrow.

Figure 12. NanoSIMS and FIB-SEM grain alignment and Pt fiducial marker placement for DOM-39. a-b) NanoSIMS $\delta^{17}\text{O}$ and $\delta^{18}\text{O}$ maps of DOM-39, with legend at right of image in units of per mil (‰). c) $\delta^{18}\text{O}$ map showing the location of the anomalous grain with semi-transparent overlay of the corresponding SE NanoSIMS image. d) NanoSIMS $\delta^{18}\text{O}$ map with semi-transparent overlay of the SE FIB-SEM image confirming the correct alignment of DOM-39. e) SE image with aligned anomalous region outlined in red, dotted yellow line indicates FIB transect. f) SE image of Pt fiducial markers with the DOM-39 grain fiducial indicated by red arrow. Distances between fiducial markers labeled. g) SE image of protective C capping layer before FIB trenching and liftout. h) HAADF STEM image of the FIB section containing DOM-39 with distances between markers labeled and grain fiducial indicated by red arrow.

Figure 13. EDS data from the footprint region of DOM-39. (a) HAADF image of the footprint region in DOM-39 with rim indicated by arrows. (b) TEM image of oriented iron sulfide crystal at a 5.7° tilt about the sample rod axis (t_x) and 2.7° tilt normal to it (t_y). (c-h) False color EDS maps of footprint region in DOM-39 for Fe, O, Mg, Si, S, and Ni, respectively. (i-k) SAED patterns obtained from regions labeled (i), (j), and (k) in TEM image.